POLYTECHNIC OF TURIN

Master of Science in Mathematical Engineering

A NUMERICAL STUDY ON A NEW BIO-INSPIRED MICRO-ROBOT

Candidate
Alberto Lolli

Academic year 2021-2022

Acknowledgments

Contents

Abstract

The objective of this study is to model and simulate the equations of motion for a conceptual prototype of micro-robot powered by four propellers made of rigid helices and of a cargo head shaped as an ellipsoid. A finite element code has been developed, intended to simulate the Stokes flow in order to derive the hydrodynamic resistance coefficients by comparing them with those present in the literature. To achieve this as reliably as possible, benchmark cases are studied using a sphere and an ellipsoid whose coefficients can be obtained through analytical formulae. The solutions of these two cases allow to compare the streamlines, the velocity and pressure fields used to validate the code. Finally, the dynamics of the problem was solved using the coefficients calculated with the code to obtain the solutions that physically represent the translational and rotational velocities of the micro-robot. Assuming that the angular velocity and the chirality of the propellers are known and can be prescribed, an analysis was made to investigate how different combinations of these can affect the translational and rotational velocities of the micro-robot and therefore the trajectory. This was done with the perspective of being able, in the future, to have a greater control on these devices and to be capable to use them for different tasks.

Chapter 1

Introduction

In recent decades, robotic research has pushed itself into the world of micro scales. This has been allowed by an advance in micro-machining and microscopic techniques which allowed us to mimic the behaviour of some biological organisms with robotic systems.

Micro-robots are expected to be increasingly present in many scientific environments, in particular a great interest is shown by the biomedical field, for instance for targeted drug delivery or highly precise microsurgery, which can lead to less invasive operations.

In the same way as in any other engineering context, it is necessary to correctly understand the physical aspects lying behind the phenomena we wish to analyse, in order to build a robust mathematical model and then implement it using numerical methods.

In the present dissertation, the problem we are going to deal with is the study of a micro-robot, sketched in figure 1.1, that moves in a highly viscous fluid. The propulsive force of this system derives from the screwing of the propellers (shown in red) around their axis. This choice is not random, but it is rather dictated by the nature of the flow. Indeed, since the movement of the micro-robot happens in a viscous fluid at a very low Reynolds number, hence the inertial forces can be neglected, the type of motion needed to generate the required thrust is not the same as one would intuitively think of in common engineering applications, such as a reciprocating motion. To sum things up, the screwing of the propellers produces a rotational and translational velocities that are transmitted to the body of the robot generating a propulsive force, allowing motion of the device. For more details on phenomena at low Reynolds number the reader can refer to [1]-[5]. Generally the motion of these devices is helicoidal, just like that showed in [40]. Our aim is to reduce the wobbling around the z axis, that is, making the trajectory more like a straight line. In order to do that we propose a new prototype of micro-swimmer composed by four propellers distanced by an eccentricity from the longitudinal axis. In *chapter* 3 we introduce kinematic and dynamic models able to describe our new micro-robot and in *chapter* 4 numerical simulations are performed using such models. Finally in the last section we try to investigate how to reduce wobbling using different propulsive configurations.

Let us now briefly describe the microswimmer as composed of two parts: the hull $\mathcal{B}_{hull}$, which is the body of the microswimmer, and the propulsive system $\mathcal{B}_{Pi}$, made up of rotating helices. It must be remarked that between the two parts no translation is allowed, therefore the only possible movement is represented by a relative rotation between the propellers and the hull with respect to the axis along the unit vector $\hat{e}_3$.
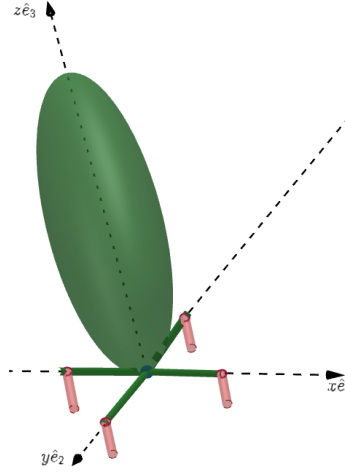

Figure 1.1: 3D microrobot model sketch

Below, the details on the composition of the parts are presented. More precisely, the hull is modelled as a rigid prolate ellipsoid with four rigid arms attached to it and the propulsive system consists of four rigid corkscrew propellers, distanced from the longitudinal axis, with unit vector $\hat{e}_3$, by an eccentricity due to the arm length,

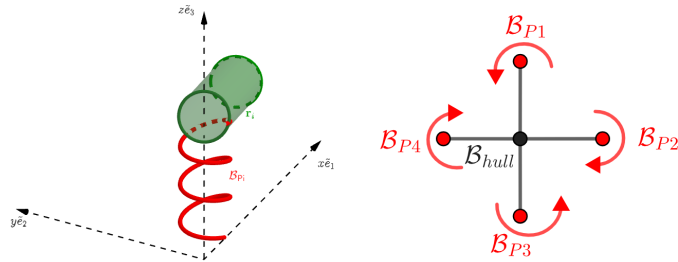Figure 1.2: 1) propeller details 2) top view of the total system

Figure 1.2 shows on the left the detailed representation of the i-th propeller (red) connected by the stiff rod to the hull (green), and on the right we can observe the overall system with, in red, the four propellers, whose angular velocities must be chosen such that the total torque acting on the body is zero in view of the null inertia hypothesis.

Chapter 2

Preliminaries

2.1 Fluid dynamics

In this section we want to illustrate the hypothesis that lead us to use the mathematical model adopted in *Chapter* 3. Recalling a formulation for the Navier-Stokes equations

$$\begin{cases} \frac{\partial}{\partial t}\rho + \nabla \cdot (\rho \mathbf{u}) = 0 \\[2mm] \frac{\partial}{\partial t}\rho \mathbf{u} + \rho(\mathbf{u} \cdot \nabla)\mathbf{u} + \mathbf{F}_{vol} = -\nabla p + \mu \Delta \mathbf{u} \end{cases} \tag{2.1}$$

It is noticeable that we do not care about boundary conditions in this section.

Assuming ρ constant in space and time, and different from 0, we can divide by ρ both members of the equation (2.1) obtaining the well-known formulation for incompressible flow

$$\begin{cases} \nabla \cdot \mathbf{u} = 0 \\[2mm] \frac{\partial}{\partial t}\mathbf{u} + (\mathbf{u} \cdot \nabla)\mathbf{u} + \frac{\mathbf{F}_{vol}}{\rho} = -\nabla(\frac{p}{\rho}) + \nu \Delta \mathbf{u} \end{cases} \tag{2.2}$$

where $\mathbf{u}(\mathbf{x}, t), p(\mathbf{x}, t)$ are the fields describing the velocity and pressure distributions inside the fluid volume V, $\mathbf{F}_{vol}$ represents the volume force and ν is the kinematic viscosity. Given the appropriate scales for the variables and proceeding with normalization

$$\tilde{\mathbf{x}} = \tfrac{\mathbf{x}}{L}; \qquad \tilde{\mathbf{u}} = \tfrac{\mathbf{u}}{U}; \qquad \tilde{t} = \tfrac{tU}{L}; \qquad \tilde{p} = \tfrac{pL}{\mu U}$$

one get the normalized Navier-Stokes equations

$$\begin{cases} \nabla \cdot \tilde{\mathbf{u}} = 0 \\[2mm] \frac{\partial}{\partial \tilde{t}}\tilde{\mathbf{u}} + (\tilde{\mathbf{u}} \cdot \nabla)\tilde{\mathbf{u}} + \tilde{\mathbf{F}}_{vol} = -\nabla \tilde{p} + \frac{1}{\mathcal{R}e}\Delta \tilde{\mathbf{u}} \end{cases} \tag{2.3}$$

The first assumption regards the stationarity of the flow, in fact, when you're dealing with microscale object time variations occur too slowly.

The second and stronger hypothesis is the negligibility of inertial terms. This is motivated from the fact that the hydrodynamic regime is identified with low $\mathcal{R}e$ number.

$$\begin{cases} \nabla \cdot \tilde{\mathbf{u}} = 0 \\[2mm] -\nabla \tilde{p} + \frac{1}{\mathcal{R}e} \Delta \tilde{\mathbf{u}} = 0 \end{cases} \tag{2.4}$$

2.2 Continuum mechanics

Follow [9] we tried to give a continuum mechanical framework in order to derive an appropriate kinematic model for the body which satisfy our expectations.

Considering the entire body as a continuum $\mathcal{B}(t)$ in a reference configuration, such that a point $\mathbf{p} \in \mathcal{B}(t)$ is a material point. Mathematically we can describe the deformation of $\mathcal{B}(t)$ through a map $\mathbf{f}$, invertible and differentiable, which carries each point $\mathbf{p}$ in $\mathbf{x} \in \mathcal{B}^*(t)$ that represents the deformed body configuration

$$\mathbf{f} : \mathcal{B} \to \mathcal{B}^* \mid \mathbf{x} = \mathbf{f}(\mathbf{p}) \tag{2.5}$$

Using the definition of deformation tensor

$$\mathbb{F} = \nabla \mathbf{f} \tag{2.6}$$

we focus our attention to the homogeneous deformation, i.e. $\mathbb{F}$ constant, and write a generic deformation as follow

$$\mathbf{f}(\mathbf{p}) = \mathbf{f}(\mathbf{q}) + \mathbb{F}(\mathbf{p} - \mathbf{q}) \qquad \forall \mathbf{p}, \mathbf{q} \in \mathcal{B} \tag{2.7}$$

Thanks to polar decomposition theorem is it possible to write $\mathbb{F} = \mathbb{Q}\mathbb{U}$. Hence, we can read the distortion as composed by a rotation, induced by tensor $\mathbb{Q}$, and a stretching described by $\mathbb{U}$ which is set to the identity tensor for our purpose. Then this deformation lead to this motion

$$\mathbf{f}(\mathbf{p}) = \mathbf{f}(\mathbf{q}) + \mathbb{Q}(\mathbf{p} - \mathbf{q}) \qquad \forall \mathbf{p}, \mathbf{q} \in \mathcal{B} \tag{2.8}$$

and the variation of the lagrangian velocity $\mathbf{v}(\mathbf{p}) = \frac{\partial \mathbf{f}(\mathbf{p})}{\partial t}$ is described by

$$\mathbf{v}(\mathbf{p}) = \mathbf{v}(\mathbf{q}) + \mathbb{A}(\mathbf{p} - \mathbf{q}) \qquad \forall \mathbf{p}, \mathbf{q} \in \mathcal{B}, \tag{2.9}$$

where $\mathbb{A}$ is a skew tensor relates to the orientation of the body in the space which axial vector is identified by the angular velocity $\mathbf{\Omega}$ of the body itself; hence we can write the angular momentum equation:

$$\boldsymbol{\alpha} = \int_{\mathcal{B}} \mathbf{r} \times \mathbf{v} \, \rho \, dV \tag{2.10}$$

Assuming that $\mathbf{G}$, the center of gravity of $\mathcal{B} = \mathcal{B}_1 \cup \mathcal{B}_2$ is aligned on the same vertical axis passing through both center of the parts , we define $\mathbf{r} = \mathbf{G}_1 - \mathbf{G}_2$ where $\mathbf{G}_i$ is the barycenter of the i-th body part, such that $\mathbf{r}$ is parallel to $\dot{\mathbf{G}}$.

Applying the definition of derivative of a vector in a rotating reference frame and using the definition of $\mathbb{J} \in \mathbb{R}^{3,3}$ as the inertial tensor in the body frame, the following balance law is found:

$$\mathbf{N} = \frac{d\boldsymbol{\alpha}}{dt}\bigg|_{\text{Inertial}} = \dot{\boldsymbol{\alpha}} + \boldsymbol{\Omega} \times \boldsymbol{\alpha} = \mathbb{J} \, \dot{\boldsymbol{\Omega}} + \boldsymbol{\Omega} \times \mathbb{J}\boldsymbol{\Omega} \tag{2.11}$$

Now we want to prove the last equality in (2.11), break up the cross product in (2.10) along the axis, one can write

$$\mathbf{r} \times \mathbf{v} = \mathbf{r} \times (\dot{\mathbf{G}} + \boldsymbol{\Omega} \times \mathbf{r}) = \mathbf{r} \times (\boldsymbol{\Omega} \times \mathbf{r})$$
$$= r_2^2(\Omega_1\hat{e}_1 + \Omega_3\hat{e}_3) + r_1^2(\Omega_2\hat{e}_2 + \Omega_3\hat{e}_3) + r_3^2(\Omega_1\hat{e}_1 + \Omega_2\hat{e}_2) - r_1r_2(\Omega_2\hat{e}_1 + \Omega_1\hat{e}_2)$$
$$= [(r_2^2 + r_3^2)\Omega_1 - \Omega_2r_2r_1 + \Omega_3r_3r_1]\hat{e}_1 + [(r_1^2 + r_3^2)\Omega_2 - \Omega_1 + \Omega_3r_2r_3]\hat{e}_2$$
$$+ [(r_1^2 + r_2^2)\Omega_3 - \Omega_2r_1r_3 + \Omega_3r_3r_2]\hat{e}_3 \tag{2.12}$$

distinguish the inertial and centrifugal moment we recognize the expression

$$\boldsymbol{\alpha} = \int_{\mathcal{B}_t} [J_1\Omega_1 - J_1'\Omega_2 - J_2'\Omega_3]\hat{e}_1 \; dV$$
$$+ \int_{\mathcal{B}_t} [-J_1'\Omega_1 + J_2\Omega_2 - J_3'\Omega_3]\hat{e}_2 \; dV + \int_{\mathcal{B}_t} [-J_2'\Omega_1 - J_3'\Omega_2 - J_3\Omega_3]\hat{e}_3 dV$$
$$\boldsymbol{\alpha} = \mathbb{J} \, \boldsymbol{\Omega} \tag{2.13}$$

Computing the cross product in (2.11)

$$\boldsymbol{\Omega} \times \boldsymbol{\alpha} = \begin{vmatrix} \hat{e}_1 & \hat{e}_2 & \hat{e}_3 \\ \Omega_1 & \Omega_2 & \Omega_3 \\ J_1\Omega_1 & J_2\Omega_2 & J_3\Omega_3 \end{vmatrix}$$

$$= [J_3\Omega_3\Omega_2 - J_2\Omega_3\Omega_2]\hat{e}_1 + [J_1\Omega_1\Omega_3 - J_3\Omega_3\Omega_1]\hat{e}_2 + [J_2\Omega_2\Omega_1 - J_1\Omega_1\Omega_2]\hat{e}_3 \tag{2.14}$$

and by adding results (2.12) with (2.14), use $\dot{\boldsymbol{\alpha}} = \mathbb{J} \, \dot{\boldsymbol{\Omega}}$ ($\mathbb{J}$ is time-independent) one has:

$$\begin{cases} N_1 = J_1\dot{\Omega}_1 + J_3\Omega_3\Omega_2 - J_2\Omega_2\Omega_3 \\ N_2 = J_2\dot{\Omega}_2 + J_1\Omega_1\Omega_3 - J_3\Omega_3\Omega_1 \\ N_3 = J_3\dot{\Omega}_3 + J_2\Omega_2\Omega_1 - J_1\Omega_1\Omega_2 \end{cases} \tag{2.15}$$

(2.15) describes the motion of the body induced by the velocity field in (2.9) which can be expressed in compact vectorial form:

$$\mathbf{N} = \mathbb{J} \, \dot{\boldsymbol{\Omega}} + \boldsymbol{\Omega} \times \boldsymbol{\alpha} \tag{2.16}$$

In order to get the equation governing the translation, it is mandatory to introduce the linear momentum equation:

$$\mathbf{l} = \int_{\mathcal{B}_t} \mathbf{v}\,\rho\,dV \tag{2.17}$$

whose balance law is

$$\mathbf{F} = \dot{\mathbf{l}} \tag{2.18}$$

where $\mathbf{F}$ is the resultant of the forces acting on the body which can be identified by two components: superficial forces, $\mathbf{F}_{sup}$ and volume forces, $\mathbf{F}_{vol}$.
Then we can write equation (2.18) as follow

$$\int_{\mathcal{B}_t} \dot{\mathbf{v}}\rho dV = \int_{\partial\mathcal{B}_t} \mathbf{s}dA + \int_{\mathcal{B}_t} \mathbf{b}dV \tag{2.19}$$

from Cauchy theorem we know that

$$\mathbf{s} = \mathbb{T}\mathbf{n} \tag{2.20}$$

then applying Gauss theorem one has

$$\int_{\mathcal{B}_t} \dot{\mathbf{v}}\rho dV = \int_{\mathcal{B}_t} \nabla \cdot \mathbb{T} + \mathbf{b}dV \tag{2.21}$$

where $\mathbb{T}$ is a second order tensor strictly dependent on the fluid properties that in this case are isotropic and newtonian, which can always be decomposed into

$$\mathbb{T}_{ij} = \mathbb{T}_{ij,eq} + \mathbb{T}_{ij,dis} = p\delta_{ij} - 2\mu\mathbb{D}_{ij} + \mu_1\mathbb{D}_{kk}\delta_{ij} \tag{2.22}$$

the first term of (2.22) is isotropic and consider the normal component of the stress tensor, i.e. the thermodynamic pressure, $\mathbb{D} \in \mathbb{R}^{3,3}$ represents the deformation velocity tensor, linear in the velocity gradient and μ, μ_1 are called Lamè coefficients which are function of the fluid composition and temperature and physically represent the viscosities which can be related through

$$\eta_{vol} = \frac{2}{3}\mu + \mu_1 \tag{2.23}$$

using Stokes hypothesis one can write the stress tensor $\mathbb{T}$ as follow

$$\mathbb{T}_{ij} = p\delta_{ij} + 2\mu\left(\mathbb{D}_{ij} - \frac{\mathbb{D}_{kk}\delta_{ij}}{3}\right) \tag{2.24}$$

where μ is the viscosity of the fluid and can be obtained experimentally.
For what concern the volume forces, we can assume two types of these: gravity and the buoyant forces applied onto the submerged object; physically these oppose each other then we can also assume that these are equal in modulus and get rid of them, having:

$$\mathbf{F} = m\ddot{\mathbf{r}} \tag{2.25}$$

Chapter 3

Mathematical model of the microswimmer

3.1 Kinematic model

A rigid body is characterized by the fact that the distance between two points within it remains constant. Moreover, its motion is composed by a translation, which can be specified by giving the coordinates of the point of interest, such as the origin $\mathcal{G}$, and a rotation tensor $\mathbb{Q}$ which depicts the body configuration in the Euclidean space.

Let us set an orthogonal coordinate system fixed on the microswimmer, known as "body frame", whose origin is in $\mathcal{O}$, at the intersection between the hull and the two axes of symmetry of the propulsion system, as shown in the figure 1.2 b). The basis of this coordinate system is indicated by the unit vectors $\{\hat{e}'_1, \hat{e}'_2, \hat{e}'_3\}$. Consider this as a time-independent coordinate system which moves as one with the body. Now, let us introduce another orthogonal reference frame, with origin in $\mathcal{G}$ called "lab frame", which is time-dependent, with unit vectors $\{\hat{e}_1(t), \hat{e}_2(t), \hat{e}_3(t)\}$. It is important to underline that the basis vectors of the body frame are parallel to the principal axes of inertia. This means that we are able to write the inertia tensor in a diagonal form along the microswimmer's body frame basis.

Mathematically speaking, we can represent this change of frame by the following relation

$$\hat{e}_i(t) = \mathbb{Q}(\boldsymbol{\alpha}(t))\hat{e}'_i \quad \forall\, i = 1, 2, 3 \tag{3.1}$$

where $\boldsymbol{\alpha}(t) = [\phi(t), \theta(t), \psi(t)]$ is the vector containing the Euler angles and describes how the body frame is positioned in the Euclidean space with respect to the lab frame. The tensor $\mathbb{Q}$ must belong to the subgroup of the orthogonal group $O(3)$:

$$SO(3) := \{\mathbb{Q} \in \mathbb{R}^{3,3} \mid \mathbb{Q}\mathbb{Q}^T = \mathbb{Q}^T\mathbb{Q} = \mathbb{I}, \ det(\mathbb{Q}) = 1\}. \tag{3.2}$$

7

The tensor $\mathbb{Q}$ is composed of three rotations: first, by an angle ϕ around the unit vector $\hat{e}'_3$, followed by a rotation θ around the unit vector $\hat{e}'_1$ and finally by ψ around $\hat{e}'_3$ again. In literature this choice is indicated as ZXZ convention. By bearing in mind that the decomposition of tensor $\mathbb{Q}$ into three rotation matrices is not a unique choice, we followed [11] to get

$$\mathbb{Q}(\phi, \theta, \psi) = \begin{bmatrix} c_\phi c_\psi - s_\phi c_\theta s_\psi & -c_\phi s_\psi - s_\phi c_\theta c_\psi & -s_\phi s_\theta \\ s_\phi c_\psi + c_\phi c_\theta s_\psi & -s_\phi s_\psi + c_\phi c_\theta c_\psi & -c_\phi s_\theta \\ s_\theta s_\psi & s_\theta c_\psi & c_\theta \end{bmatrix} \tag{3.3}$$

where the temporal dependency is omitted to simplify to a shorthand notation. Furthermore this tensor is function of a scalar value $t \in \mathbb{R}_+$, hence differentiating with respect to time, the first condition that characterize the space defined in (3.2), one has

$$\dot{\mathbb{Q}}\mathbb{Q}^T + \mathbb{Q}\dot{\mathbb{Q}}^T = \mathbb{O} \tag{3.4}$$

where $\mathbb{O}$ is the tensor of zero elements. In (3.4) it is possible to rename the first of the two matrices product as

$$\mathbb{A} = \dot{\mathbb{Q}}\mathbb{Q}^T \tag{3.5}$$

This is a skew tensor that guarantees for each vector $\mathbf{v}$ the following property

$$\mathbb{A}\mathbf{v} = \boldsymbol{\Omega} \times \mathbf{v} \tag{3.6}$$

where $\boldsymbol{\Omega} = [\Omega_1, \Omega_2, \Omega_3]$ is the axial vector associated to the matrix $\mathbb{A}$ which can be written as

$$\mathbb{A} = \begin{bmatrix} 0 & -\Omega_3 & \Omega_2 \\ \Omega_3 & 0 & -\Omega_1 \\ -\Omega_2 & \Omega_1 & 0 \end{bmatrix} \tag{3.7}$$

thus, $\mathbb{A}$ can be defined by three parameters, called angular velocities of $\mathcal{G}$, which are assumed to be coincident with $\boldsymbol{\Omega}_{hull} = [\Omega_{h,1}, \Omega_{h,2}, \Omega_{h,3}]^T \in \mathbb{R}^3$, i.e. the angular velocities of the hull system, illustrated in 3.1.

From the knowledge of $\boldsymbol{\Omega}_{hull}$, through (3.5), we can estimate the Euler angles solving the ordinary differential equation for the rotation of a body

$$\dot{\mathbb{Q}}\mathbf{r}'_i = \dot{\mathbb{Q}}\mathbb{Q}^T \mathbb{Q}\mathbf{r}'_i = \mathbb{A}\mathbb{Q}\mathbf{r}'_i = \boldsymbol{\Omega}_{hull} \times \mathbb{Q}\mathbf{r}'_i \tag{3.8}$$

where $\mathbf{r}'_i \in \mathbb{R}^3$ is the hull's arm length expressed in the body frame $\mathcal{O}$ and showed in figure 1.2.

It is convenient to assume that the body frame $\mathcal{O}$ coincides with the initial configuration of $\mathcal{B}(t) \equiv \mathcal{B}(t = 0)$ and the lab frame is evolving in time with respect to this one through the map formalized in (2.5). A classical law, valid for rigid body approximation only, is used in order to describe such unknown function, i.e.

$$\overline{\mathcal{O}P_i}(t) = \overline{\mathcal{O}\mathcal{G}}(t) + \mathbb{Q}(\boldsymbol{\alpha}(t))\mathbf{r}'_i \quad \forall i = 1, \dots, 4 \tag{3.9}$$

Figure 3.1 shows a sketch of the problem: in the kinematic analysis it is possible to neglect masses and shapes which do not account of the position and velocities of the system, so the microswimmer is described through stiff rods instead of its real geometry and the considerations that follows are valid with respect to the reference systems described previously.
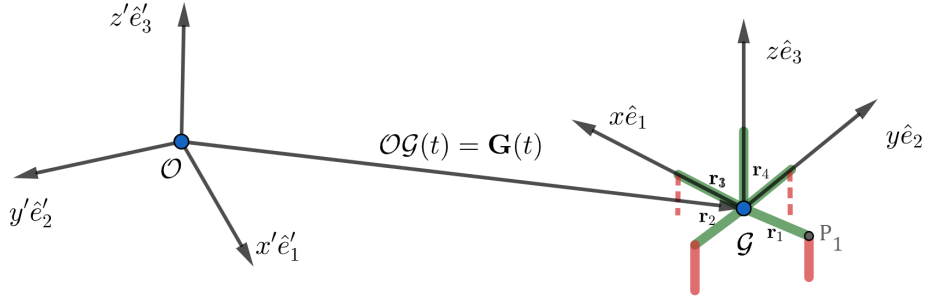

Figure 3.1: Kinematic model of the swimmer - the green represents $\mathcal{B}_{hull}$ and the red $\mathcal{B}_{Pi}$

3.1.1 Hull system kinematic

For ease of notation we rename $\overline{\mathcal{O}P_i}(t) = \mathbf{p}_i(t) \in \mathbb{R}^3$ the vector that describes the location of the point located on the hull's extremity, where $p_i \in \mathcal{B}_{hull}(t)$ and $\overline{\mathcal{O}\mathcal{G}}(t) = \mathbf{G}(t) \in \mathbb{R}^3$ to identify the position of the center of gravity in the lab frame. Equation (3.9) becomes

$$\mathbf{p}_i(t) = \mathbf{G}(t) + \mathbb{Q}(\boldsymbol{\alpha}(t))\mathbf{r}'_i \quad \forall i = 1, \dots, 4 \tag{3.10}$$

For what concerns the center of gravity we want to remark that in the whole thesis it is assumed to be coincident with the intersection point between the ellipsoid and the four rods. In reality, this is not true, as a matter of fact the dimensions and orientation of the propellers influence the position of the center of mass by lowering it along the same axis, due to the symmetrical setting of the propellers.

$$\mathbf{G}(t) = \frac{\mathbf{G}_{hull}(t) + \sum_{i=1}^{4} \mathbf{G}_{Pi}(t)}{2} \approx \mathcal{G} \tag{3.11}$$

where $\mathbf{G}_{hull}$ is the hull's center of mass and $\mathbf{G}_{Pi}$ is that of the $i-$th propeller. The reality is slightly different but in this first approximation we are satisfied with such hypothesis.
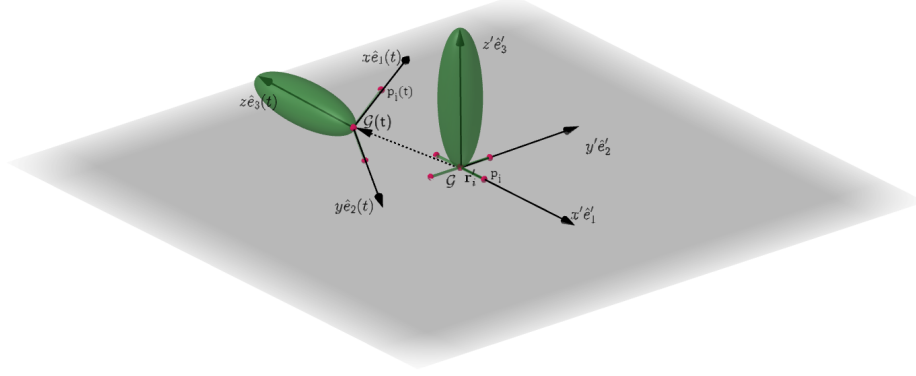
Figure 3.2: Rototranslation of $\mathcal{B}_{hull}$ over a period of time Δ_t

The microswimmer kinematics involves angular and translational velocity for all body parts, then to describe its motion we need to identify both sources. Deriving equation (3.10) we get the velocity of a point which lies in the hull's extremity

$$\dot{\mathbf{p}}_i(t) = \mathbf{U}_{Pi}(t) = \dot{\mathbf{G}}(t) + \dot{\mathbb{Q}}(\boldsymbol{\alpha}(t))\mathbf{r}'_i = \dot{\mathbf{G}}(t) + \mathbb{A}\mathbb{Q}\mathbf{r}'_i = \dot{\mathbf{G}}(t) + \boldsymbol{\Omega}_{hull}(t) \times \mathbb{Q}\mathbf{r}'_i \qquad (3.12)$$

Through this formula it is possible to conclude that the translational velocity of the center of gravity is $\dot{\mathbf{G}}(t)$, while elements which do not stand along the $z-$axis also have a contribution which is directly proportional to their distance from it, related with the angular velocity of the hull $\boldsymbol{\Omega}_{hull}$. It is pointed out that this latter enrichment is the maximum for the chosen point $\mathbf{p}_i$.

3.1.2 Propellers system kinematic

Since all the propellers are identical, we can restrict our attention to only one of them and extend the reasoning to the others. The propeller can rotate only along $\tilde{z}-$axis with angular velocity $\boldsymbol{\omega}(t)$ and it moves jointly with the hull because it is connected to the extremity point p_i. Each propeller has its own reference system centered in $\mathcal{O}_p$ with axes directed along $\tilde{e}_i$ and its spatial orientation is fully described by tensor $\mathbb{Q}_p$ which has the same properties of $\mathbb{Q}$, but represents only a $\tilde{z}-$ rotation. It must be remarked that $\tilde{z}$ and z are parallel at each time.

$$\boldsymbol{\omega}_i(t) = \frac{d\beta_i}{dt}\tilde{e}_3(t) = \omega_i \mathbb{Q}_p \tilde{e}'_3 \qquad (3.13)$$

where β_i is the angle associated to ω_i, which represents the angular velocity from the lab frame point of view, and it is a model parameter. Finally, the whole kinematics of $\mathcal{B}(t)$ is
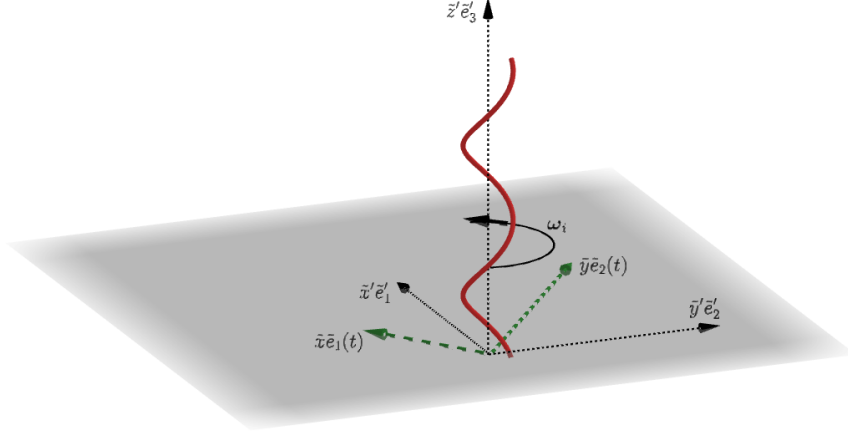
Figure 3.3: Rotation of the propeller over a period of time Δ_t

described in the next section for a full comprehension of the kinematics, providing velocities relations of the individual parts with respect to each other.

3.1.3 Composite kinematics

Choosing a generic point q_i on the $i-$th propeller we can estimate its initial position with respect to the point p_i previously described simply by the vector

$$\tilde{\mathbf{r}}_i(0) = \mathbf{q}_i(0) - \mathbf{p}_i(0) \tag{3.14}$$

then we have that its position with respect to the center of gravity is given by

$$\mathbf{q}_i(t) = \mathbf{p}_i(t) + \mathbb{Q}\mathbb{Q}_p \tilde{\mathbf{r}}_i(0) \tag{3.15}$$

and remembering that the transformation from the initial state to the actual configuration is made thanks to the application of the rotation tensors $\mathbb{Q}$ and $\mathbb{Q}_p$. Differentiating with respect to time (3.15) we get the velocity of a generic point on the propeller

$$\dot{\mathbf{q}}_i(t) = \dot{\mathbf{p}}_i(t) + \dot{\mathbb{Q}}\mathbb{Q}_p \tilde{\mathbf{r}}(0) + \mathbb{Q}\dot{\mathbb{Q}}_p \tilde{\mathbf{r}}(0) \tag{3.16}$$

and applying to $\dot{\mathbb{Q}}_p$ the rule deduced in (3.8) we get the following result

$$\dot{\mathbf{q}}_i(t) = \dot{\mathbf{p}}_i(t) + \boldsymbol{\Omega}_{hull} \times (q_i(t) - p_i(t)) + \boldsymbol{\omega}_i(t) \times (q_i(t) - p_i(t))$$

11

$$= \dot{\mathbf{p}}_i(t) + (\mathbf{\Omega}_{hull} + \boldsymbol{\omega}_i) \times (q_i(t) - p_i(t)) \tag{3.17}$$

where $\boldsymbol{\omega_i}(t)$ is the axial vector of $\dot{\mathbb{Q}}_p \mathbb{Q}_p$ described in (3.13). Now, we are finally able to exploit the total angular velocity of the propeller

$$\mathbf{\Omega}_i = \mathbf{\Omega}_{hull} + \boldsymbol{\omega}_i \tag{3.18}$$

3.2   Fluid model

The small size of the object and the high viscosity of the fluid in which it moves lead to a low Reynolds regime, for which the well-known Stokes equations apply.

$$\begin{cases} \nabla \cdot \mathbf{u}(\mathbf{x}) = 0 \quad \forall \mathbf{x} \in \mathcal{V} \backslash \mathcal{B} \\\\ -\nabla p(\mathbf{x}) + \nu \Delta \mathbf{u}(\mathbf{x}) = 0 \quad \forall \mathbf{x} \in \mathcal{V} \backslash \mathcal{B} \\\\ \mathbf{u}(\mathbf{x}), p(\mathbf{x}) \to 0 \quad \text{for } \|\mathbf{x}\| \to +\infty \\\\ \mathbf{u}(\mathbf{x}) = \mathbf{v}(\mathbf{q}) \quad \forall\, \mathbf{x}, \mathbf{q} \in \partial\mathcal{B} \end{cases} \tag{3.19}$$

where $\mathcal{V}$ is the volume of the fluid surrounding the body $\mathcal{B}$, $\mathbf{u}(\mathbf{x}) \in \mathbb{R}^3$, $p(\mathbf{x}) \in \mathbb{R}$ are the velocity and pressure fields of the fluid, respectively, while $\nu \in \mathbb{R}$ represents the viscosity, $\mathbf{v} \in \mathbb{R}^3$ is the velocity vector field derived in (3.12). Note that (3.19) is a linear system for which exists a solution and it models the fluid behavior.

Now we will derive a variational formulation for the Stokes system described in (3.19) and without loss of generality we consider unitary viscosity.

Let $V = \{v \in H^1(\mathcal{V}) : v|_{\mathcal{V}} = 0\}$ and $Q = \{q \in L_2(\mathcal{V}) : q|_{\mathcal{V}} = 0\}$ two Hilbert spaces containing the test function (v, q), the variational problem can be expressed as follows, find $(u, p) \in V \times Q$ such that:

$$\begin{cases} \int_{\mathcal{V}} \nabla \mathbf{u} \cdot \nabla \mathbf{v} \, dx - \int_{\mathcal{V}} (\nabla \cdot \mathbf{v}) p \, dx = 0 \\\\ \int_{\mathcal{V}} (\nabla \cdot \mathbf{u}) q \, dx = 0 \end{cases} \tag{3.20}$$

or in compact form

$$\begin{cases} a(u, v) + b(v, p) = 0 \\ b(u, q) = 0 \end{cases} \tag{3.21}$$

$\forall (v, q) \in V \times Q$.

3.3 Dynamic model

At this point it is mandatory to derive a method in order to compute the force and the moment (respect to $\mathbf{G}$) that the fluid applies on the body, indicated with $\mathbf{F}$ and $\mathbf{N}$. It is well known that this forces depends linearly from the velocities in view of Stokes hypothesis and are highly influenced by the geometry of the solid and the fluid properties around it. The first step is to consider a rigid sphere then, from the literature, we can write

$$\begin{cases} \mathbf{F} = -6\pi\mu r\mathbb{I}\mathbf{U} \\ \mathbf{N} = -8\pi\mu r^3\mathbb{I}\mathbf{\Omega} \end{cases} \tag{3.22}$$

where μ is the kinematic viscosity of the fluid, r is the radius, $\mathbb{I} \in \mathbb{R}^{3,3}$ is the identity tensor applied to $\mathbf{U} \in \mathbb{R}^3$, $\mathbf{U} = [U_1, U_2, U_3]^T$ the linear velocity and $\mathbf{\Omega} \in \mathbb{R}^3$, $\mathbf{\Omega} = [\Omega_1, \Omega_2, \Omega_3]^T$ the angular one. It is observed that an object which translates and rotates around some axes is affected by a hydrodynamic resistance in terms of force and torque. Since the governing equations are linear we can decompose the problem into two simpler challenges: translation characterized by $\mathbf{U}$ and rotation due to $\mathbf{\Omega}$. Hence we can write in a general framework the following equation

$$\mathbf{F} = -\mu\mathbb{K}\mathbf{U} \tag{3.23}$$

where $\mathbb{K}$ is a second order symmetric matrix closely dependent from the geometry of the body; we should call "translation tensor". The torque can be expressed as

$$\mathbf{N} = -\mu\mathbb{W}^O\mathbf{\Omega} \tag{3.24}$$

where $\mathbb{W}^O$ is a second order symmetric matrix subsequently called "rotational tensor". The apex O stands for the origin of the axis of rotation, so this tensor is point-dependent; furthermore, an interesting property is that the three eigenvectors of $\mathbb{K}$ ($\mathbb{W}^O$) are parallel to the principal axis of translational (rotational) resistance.

Real motion of a six-degree of freedom body, which is both translating and rotating, is given by the following dynamics

$$\begin{cases} \mathbf{F} = -\mu\mathbb{K}\mathbf{U} - \mu\mathbb{C}^O\mathbf{\Omega} \\ \mathbf{N} = -\mu\mathbb{C}^O\mathbf{U} - \mu\mathbb{W}^O\mathbf{\Omega} \end{cases} \tag{3.25}$$

where $\mathbb{C}^O$ is a second order non symmetric coupling tensor. It is noteworthing that it can be symmetric in only one specific point called center of hydrodynamic reaction.

The previously discussion has a generic undertone, then we intend to explicitly derive a representation of these tensors for our specific case and we start with a hull's description. The body $\mathcal{B}_{hull}$ is orthotropic i.e. has three mutually perpendicular symmetry planes. Remembering that point G is the center of gravity of $\mathcal{B}_{hull}$ and that for centrally symmetric bodies, such as ellipsoid, it coincides with the hydrodynamic reaction point, the tensors for this body part can be represented as follows

$$\mathbb{K} = \begin{bmatrix} K_{11} & 0 & 0 \\ 0 & K_{22} & 0 \\ 0 & 0 & K_{33} \end{bmatrix}, \quad \mathbb{W}^G = \begin{bmatrix} W_{11} & 0 & 0 \\ 0 & W_{22} & 0 \\ 0 & 0 & W_{33} \end{bmatrix}, \quad \mathbb{C}^G = \begin{bmatrix} 0 & 0 & 0 \\ 0 & 0 & 0 \\ 0 & 0 & 0 \end{bmatrix}. \tag{3.26}$$

As proposed in [17], to give a numerical value for the coefficients one can use

$$
\begin{cases}
K_{ii} = 16\pi \frac{1}{\chi + a_i^2 \alpha_i} & i = 1, 2, 3 \\
W_{11} = \frac{16}{3}\pi \frac{a_2^2 + a_3^2}{a_2^2 \alpha_2 + a_3^2 \alpha_3} \\
W_{22} = \frac{16}{3}\pi \frac{a_3^2 + a_1^2}{a_3^2 \alpha_3 + a_1^2 \alpha_1} \\
W_{33} = \frac{16}{3}\pi \frac{a_1^2 + a_2^2}{a_1^2 \alpha_1 + a_2^2 \alpha_2}
\end{cases}
\tag{3.27}
$$

in which

$$
\alpha_j = \int_0^\infty \frac{d\lambda}{(a_j^2 + \Delta(\lambda))}
\tag{3.28}
$$

$$
\chi = \int_0^\infty \frac{d\lambda}{\Delta(\lambda)}
\tag{3.29}
$$

where $\Delta(\lambda) = \left[(a_1^2 + \lambda)(a_2^2 + \lambda)(a_3^2 + \lambda) \right]$ and a_j stands for the semi-axis length.

Our microswimmer consists, in addition to a hull, of four identical thrusters that have been designed taking inspiration out of nature, from bacteria's tail such as E. coli for example, adopting some simplifying hypothesis such as rigidity.

It is known that screwlike structures, like that of the propellers, exhibits coupling between translation and rotation, then a reformulation of (3.26) is mandatory for all $\mathcal{B}_{Pi}$, following [18] one can write the tensors as follows

$$
\mathbb{K}_p^{(i)} = \begin{bmatrix} K_{p,11} & 0 & 0 \\ 0 & K_{p,22} & 0 \\ 0 & 0 & K_{p,33}^{(i)} \end{bmatrix}, \quad
\mathbb{W}_p^{Gp,(i)} = \begin{bmatrix} W_{p,11} & 0 & 0 \\ 0 & W_{p,22} & 0 \\ 0 & 0 & W_{p,33}^{(i)} \end{bmatrix},
$$

$$
\mathbb{C}_p^{Gp} = \begin{bmatrix} C_{p,11} & C_{p,12} & 0 \\ -C_{p,21} & C_{p,22} & 0 \\ 0 & 0 & C_{p,33} \end{bmatrix}.
\tag{3.30}
$$

where the subscript p is added in order to identifying the belonging to the propeller.

The differences between these and those described in (3.26) consist in the numerical values and in the structure of the coupling tensor, that here, is non zero.

In fact these are deduced for bodies which have a helicoidal symmetry about one axis, coincident with $\tilde{e}_3(t)$, and the coupling and rotational dyadic are computed with respect to the center of gravity of the propeller. As previously specified every body posses a particular point, called center of hydrodynamic reaction, $\mathbf{R}$, where the coupling tensor becomes diagonal

$$
\mathbb{C}_p^{R,(i)} = \begin{bmatrix} C_{p,11} & 0 & 0 \\ 0 & C_{p,22} & 0 \\ 0 & 0 & C_{p,33} \end{bmatrix}.
\tag{3.31}
$$

14

The reader is addressed to [20] in order to understand where the formula (3.32) used to compute such a point comes from

$$\mathbf{R} - \mathbf{G} = \frac{C_{p,32} - C_{p,23}}{K_{p,2} + K_{p,3}}\tilde{e}_1 + \frac{C_{p,13} - C_{p,31}}{K_{p,1} + K_{p,3}}\tilde{e}_2 + \frac{C_{p,21} - C_{p,12}}{K_{p,2} + K_{p,1}}\tilde{e}_3 \qquad (3.32)$$

where K_i is the $i-$th eigenvalue and $\tilde{e}_i$ represent the associated eigenvectors of $\mathbb{K}_p^{(i)}$, while $C_{p,ij}$ are the coefficients of the coupling tensor computed with respect to the center of mass of the propeller, $\mathbf{G}_p$.

Once we have these coefficients it is possible to solve the dynamics, after understanding how the generalized hydrodynamic forces $\mathbf{f}, \boldsymbol{\tau}$ are produced by each part of the body. Consistently with [1] we emphasize the relationship between these and the variables which define the thrust and the torque using the linear maps f, n, f_p, n_p

$$\begin{cases} \mathbf{f}_{hull} = f\big(\mathbb{K}, \mathbb{C}^G, \mathbb{Q}, \dot{\boldsymbol{G}}, \boldsymbol{\Omega}_{hull}\big) \\ \boldsymbol{\tau}_{hull} = n\big(\mathbb{W}^G, \mathbb{C}^G, \mathbb{Q}, \dot{\boldsymbol{G}}, \boldsymbol{\Omega}_{hull}\big) \\ \mathbf{f}^{(i)} = f_p\big(\mathbb{K}_p^{(i)}, \mathbb{C}_p^{R,(i)}, \mathbb{Q}, \dot{\boldsymbol{G}}, \boldsymbol{\Omega}_{hull}, \mathbf{r}^{(i)}, \boldsymbol{\omega_i}\big) \quad \forall i = 1, \dots, 4 \\ \boldsymbol{\tau}^{(i)} = n_p\big(\mathbb{W}_p^{G_p,(i)}, \mathbb{C}_p^{R,(i)}, \mathbb{Q}, \dot{\boldsymbol{G}}, \boldsymbol{\Omega}_{hull}, \mathbf{r}^{(i)}, \boldsymbol{\omega_i}\big) \quad \forall i = 1, \dots, 4 \end{cases} \qquad (3.33)$$

Combining (3.33) with the set of kinematic equations derived before, one get the formulations for the thrust and the torque in each body part produced by the motion expressed in (2.8), into the fluid

$$\begin{cases} \mathbf{f}_{hull} = \mathbb{K}\dot{\mathbf{G}}(t) + \mathbb{C}^G\boldsymbol{\Omega}_{hull} \\ \boldsymbol{\tau}_{hull} = \mathbb{C}^G\dot{\mathbf{G}}(t) + \mathbb{W}^G\boldsymbol{\Omega}_{hull} \\ \mathbf{f}^{(i)} = \mathbb{K}_p^{(i)}\big(\dot{\mathbf{G}}(t) + \boldsymbol{\Omega}_{hull} \times \mathbb{Q}\mathbf{r}_i'\big) + \mathbb{C}_p^{R,(i)}\boldsymbol{\Omega}_i \quad \forall i = 1, \dots, 4 \\ \boldsymbol{\tau}^{(i)} = \mathbb{C}_p^R\big(\dot{\mathbf{G}}(t) + \boldsymbol{\Omega}_{hull} \times \mathbb{Q}\mathbf{r}_i'\big) + \mathbb{W}_p^{G_p,(i)}\boldsymbol{\Omega}_i \quad \forall i = 1, \dots, 4 \end{cases} \qquad (3.34)$$

where $\mathbf{f}^{(i)}$ represents the force exerted by the propeller $i-$th, $\boldsymbol{\tau}^{(i)}$ is the moment computed with respect to $\tilde{z}\tilde{e}_3$ axis passing through $\mathbf{G}_p^{(i)}$; note that there is a first difference with [22] in the linear term associated to the translational velocity in both $\mathbf{f}^{(i)}$, $\boldsymbol{\tau}^{(i)}$ due to the distance from $\mathbf{G}$ of the propellers. The first two equations represent the force and the torque, with pole in $\mathbf{G}$, exerted only by the hull system.

Now we try to isolate the unknowns in order to solve the system, then calling

$$\Omega_{hull} \times \mathbb{Q}\mathbf{r}_i' = \mathbb{A}^{(i)}\mathbf{r}_i \qquad (3.35)$$

and computing $\mathbb{L}_k^{(i)} = \mathbb{K}_p^{(i)}\mathbb{A}^{(i)}$, $\mathbb{L}_c^{(i)} = \mathbb{C}_p^{R,(i)}\mathbb{A}^{(i)}$, it is possible to write more compactly

$$
\begin{cases}
\mathbf{f}^{(i)} = \underbrace{\mathbb{K}_p^{(i)}\dot{\mathbf{G}}(t) + \mathbb{L}_k^{(i)}\boldsymbol{\Omega}_{hull}}_{\text{translational contribution}} + \underbrace{\mathbb{C}_p^{R,(i),T}\boldsymbol{\Omega_i}}_{\text{rotational contribution}} & \forall i = 1,\dots,4 \\
\boldsymbol{\tau}^{(i)} = \underbrace{\mathbb{C}_p^{R,(i)}\dot{\mathbf{G}}(t) + \mathbb{L}_c^{(i)}\boldsymbol{\Omega}_{hull}}_{\text{translational contribution}} + \underbrace{\mathbb{W}_p^{G_p,(i)}\boldsymbol{\Omega_i}}_{\text{rotational contribution}} & \forall i = 1,\dots,4
\end{cases}
\tag{3.36}
$$

recovering the equations structure proposed by Puercell in [3] but with a subtle difference in the term related to linear velocity due to non coaxial position of the propellers.

A compact formulation of (3.34) is then proposed in order to guarantee a decoupling between the unknowns and the coefficients of the resistance matrices, hence

$$
\begin{cases}
\begin{bmatrix} \mathbf{f}_{hull} \\ \boldsymbol{\tau}_{hull} \end{bmatrix} = \left[\begin{array}{c|c} \mathbb{K} & \mathbb{C}^G \\ \hline \mathbb{C}^G & \mathbb{W}^G \end{array}\right] \begin{bmatrix} \dot{\boldsymbol{G}} \\ \boldsymbol{\Omega}_{hull} \end{bmatrix} \\
\begin{bmatrix} \mathbf{f}^{(i)} \\ \boldsymbol{\tau}^{(i)} \end{bmatrix} = \left[\begin{array}{c|c} \mathbb{K}_p^{(i)} & \mathbb{L}_k^{(i)} + \mathbb{C}_p^{R,T,(i)} \\ \hline \mathbb{C}_p^{R,(i)} & \mathbb{L}_c^{(i)} + \mathbb{W}_p^{G_p,(i)} \end{array}\right] \begin{bmatrix} \dot{\boldsymbol{G}} \\ \boldsymbol{\Omega}_{hull} \end{bmatrix} + \begin{bmatrix} \mathbb{C}_p^{R,(i)} \\ \mathbb{W}_p^{G_p,(i)} \end{bmatrix} \boldsymbol{\omega}_i & \forall i = 1,\dots,4
\end{cases}
\tag{3.37}
$$

Since we are working in a low Reynolds regime, the total force $\mathbf{F}$ and torque $\mathbf{N}$, acting on the whole body, $\mathcal{B}$, are zero, this is an approximation due to the fact that inertial terms are negligible than viscous one, so the second member of the balance laws (2.16),(2.25) can be overlook leading to the total forces balance on the whole body $\mathcal{B}$

$$
\begin{cases}
\mathbf{F} = \mathbf{f}_{hull} + \sum_{i=1}^4 \mathbf{f}^{(i)} = \mathbf{0} \\
\mathbf{N} = \boldsymbol{\tau}_{hull} + \sum_{i=1}^4 \left(\boldsymbol{\tau}^{(i)} + \mathbf{b}^{(i)} \right) = \mathbf{0}
\end{cases}
\tag{3.38}
$$

where $\mathbf{b}^{(i)} = \mathbf{r}^{(i)} \times \mathbf{f}^{(i)}$ is added in order to consider also the contribution to the moment, respect to $\mathbf{G}$, of the force generated by the $i-$th propeller; note that $\mathbf{r}^{(i)} = \mathbb{Q}\mathbf{r}'_i$ represents the arm length in the lab frame system.

If (3.37) is replaced into (3.38), the equations of motion are obtained

$$
\left[\begin{array}{c|c} \mathbb{K} & \mathbb{C}^G \\ \hline \mathbb{C}^G & \mathbb{W}^G \end{array}\right] \begin{bmatrix} \dot{\boldsymbol{G}} \\ \boldsymbol{\Omega}_{hull} \end{bmatrix} + \sum_{i=1}^4 \left[\begin{array}{c|c} \mathbb{K}_p^{(i)} & \mathbb{L}_k^{(i)} + \mathbb{C}_p^{R,T,(i)} \\ \hline \mathbb{C}_p^{R,(i)} & \mathbb{L}_c^{(i)} + \mathbb{W}_p^{G_p,(i)} \end{array}\right] \begin{bmatrix} \dot{\boldsymbol{G}} \\ \boldsymbol{\Omega}_{hull} \end{bmatrix} + \begin{bmatrix} \mathbb{C}_p^{R,(i)} \\ \mathbb{W}_p^{G_p,(i)} \end{bmatrix} \boldsymbol{\omega}_i + \begin{bmatrix} \mathbf{0} \\ \mathbf{b}^{(i)} \end{bmatrix} = \begin{bmatrix} \mathbf{0} \\ \mathbf{0} \end{bmatrix}
\tag{3.39}
$$

and exploiting the vector $[\mathbf{0}, \mathbf{b}^{(i)}]^T$ in (3.39)

$$
\begin{bmatrix}
\mathbf{0}^T \\
\Delta r_1^{(i)} \left\{ \sum_{n=1}^3 \left[([\mathbb{K}_p^{(i)}]_{3,n} - [\mathbb{K}_p^{(i)}]_{2,n})\dot{G}_n + ([\mathbb{L}_k^{(i)}]_{3,n} + [\mathbb{C}_p^{R,(i)}]_{3,n} - [\mathbb{L}_k^{(i)}]_{2,n} - [\mathbb{C}_p^{R,(i)}]_{2,n})\Omega_{h,n} + ([\mathbb{C}_p^{R,(i)}]_{3,n} - [\mathbb{C}_p^{R,(i)}]_{2,n})\omega_n \right] \right. \\
\Delta r_2^{(i)} \left\{ \sum_{n=1}^3 \left[([\mathbb{K}_p^{(i)}]_{1,n} - [\mathbb{K}_p^{(i)}]_{3,n})\dot{G}_n + ([\mathbb{L}_k^{(i)}]_{1,n} + [\mathbb{C}_p^{R,(i)}]_{1,n} - [\mathbb{L}_k^{(i)}]_{3,n} - [\mathbb{C}_p^{R,(i)}]_{3,n})\Omega_{h,n} + ([\mathbb{C}_p^{R,(i)}]_{1,n} - [\mathbb{C}_p^{R,(i)}]_{3,n})\omega_n \right] \right. \\
\Delta r_3^{(i)} \left\{ \sum_{n=1}^3 \left[([\mathbb{K}_p^{(i)}]_{2,n} - [\mathbb{K}_p^{(i)}]_{1,n})\dot{G}_n + ([\mathbb{L}_k^{(i)}]_{2,n} + [\mathbb{C}_p^{R,(i)}]_{2,n} - [\mathbb{L}_k^{(i)}]_{1,n} - [\mathbb{C}_p^{R,(i)}]_{1,n})\Omega_{h,n} + ([\mathbb{C}_p^{R,(i)}]_{2,n} - [\mathbb{C}_p^{R,(i)}]_{1,n})\omega_n \right] \right.
\end{bmatrix}
\tag{3.40}
$$

It is necessary to clarify the notation used above, the index i indicate the $i-$th hull's arm and $[\ \cdot\ ]_{m,n}$ stands for the component (m,n) of the generic tensor. Furthermore $\Delta r_1^{(i)} = r_2^{(i)} - r_3^{(i)}$, $\Delta r_2^{(i)} = r_3^{(i)} - r_1^{(i)}$, $\Delta r_3^{(i)} = r_1^{(i)} - r_2^{(i)}$ are constant values, so take advantage of linear algebra is it possible to represent $\mathbf{b}^{(i)} \in \mathbb{R}^3$ as $\mathbb{M}^{(i)}\mathbf{x} + \mathbb{N}^{(i)}\boldsymbol{\omega}_i = \mathbf{b}^{(i)}$. This allow us to separate the unknowns $\mathbf{x} = [\dot{\mathbf{G}}, \boldsymbol{\Omega}]^T \in \mathbb{R}^6$ from the coefficients recovering a formulation similar to (3.37) also for the last term in the first member of (3.39)

$$\begin{bmatrix} \mathbf{0} \\ \mathbf{b}^{(i)} \end{bmatrix} = \left[\begin{array}{c|c} \mathbb{0} & \mathbb{0} \\ \hline \mathbb{M}_1^{(i)} & \mathbb{M}_2^{(i)} \end{array} \right] \begin{bmatrix} \dot{\boldsymbol{G}} \\ \boldsymbol{\Omega}_{hull} \end{bmatrix} + \begin{bmatrix} \mathbb{0} \\ \mathbb{N}^{(i)} \end{bmatrix} \boldsymbol{\omega}_i \tag{3.41}$$

where $\mathbb{M}_1^{(i)} \in \mathbb{R}^{3,3}$ and $\mathbb{M}_2^{(i)} \in \mathbb{R}^{3,3}$ are such that $\mathbb{M}^{(i)} = [\mathbb{M}_1^{(i)}, \mathbb{M}_2^{(i)}]^T$, $\mathbb{N}^{(i)} \in \mathbb{R}^{3,3}$ and $\mathbb{0} \in \mathbb{R}^{3,3}$ is the tensor with all zeros. For a whole comprehension about the role of these matrices, their full structure is reported below; showing that physically these are function of the previous tensors and all the components depend on $\mathbf{r}^{(i)}$. This is confirmed by the fact that when $\mathbf{r}^{(i)}$ is zero, there is no torque component in this sense, and therefore these dyadics do not exist. We can highlight the influence of the eccentricity $\hat{e} = |\Delta r_i| = 40\ mm$

$$\mathbb{M}_1^{(i)} = \hat{e} \begin{bmatrix} ([\mathbb{K}_p^{(i)}]_{3,1} - [\mathbb{K}_p^{(i)}]_{2,1}) & ([\mathbb{K}_p^{(i)}]_{3,2} - [\mathbb{K}_p^{(i)}]_{2,2}) & ([\mathbb{K}_p^{(i)}]_{3,3} - [\mathbb{K}_p^{(i)}]_{2,3}) \\ ([\mathbb{K}_p^{(i)}]_{1,1} - [\mathbb{K}_p^{(i)}]_{3,1}) & ([\mathbb{K}_p^{(i)}]_{1,2} - [\mathbb{K}_p^{(i)}]_{3,2}) & ([\mathbb{K}_p^{(i)}]_{1,3} - [\mathbb{K}_p^{(i)}]_{3,3}) \\ ([\mathbb{K}_p^{(i)}]_{2,1} - [\mathbb{K}_p^{(i)}]_{1,1}) & ([\mathbb{K}_p^{(i)}]_{2,2} - [\mathbb{K}_p^{(i)}]_{1,2}) & ([\mathbb{K}_p^{(i)}]_{2,3} - [\mathbb{K}_p^{(i)}]_{1,3}) \end{bmatrix} \tag{3.42}$$

$$\mathbb{N}^{(i)} = \hat{e} \begin{bmatrix} ([\mathbb{C}_p^{R,(i)}]_{3,1} - [\mathbb{C}_p^{R,(i)}]_{2,1}) & ([\mathbb{C}_p^{R,(i)}]_{3,2} - [\mathbb{C}_p^{R,(i)}]_{2,2}) & ([\mathbb{C}_p^{R,(i)}]_{3,3} - [\mathbb{C}_p^{R,(i)}]_{2,3}) \\ ([\mathbb{C}_p^{R,(i)}]_{1,1} - [\mathbb{C}_p^{R,(i)}]_{3,1}) & ([\mathbb{C}_p^{R,(i)}]_{1,2} - [\mathbb{C}_p^{R,(i)}]_{3,2}) & ([\mathbb{C}_p^{R,(i)}]_{1,3} - [\mathbb{C}_p^{R,(i)}]_{3,3}) \\ ([\mathbb{C}_p^{R,(i)}]_{2,1} - [\mathbb{C}_p^{R,(i)}]_{1,1}) & ([\mathbb{C}_p^{R,(i)}]_{2,2} - [\mathbb{C}_p^{R,(i)}]_{1,2}) & ([\mathbb{C}_p^{R,(i)}]_{2,3} - [\mathbb{C}_p^{R,(i)}]_{1,3}) \end{bmatrix}$$
$$\tag{3.43}$$

Finally it is possible to rewrite the equations of motion as follows

$$\left[\begin{array}{c|c} \mathbb{K} & \mathbb{C}^G \\ \hline \mathbb{C}^G & \mathbb{W}^G \end{array} \right] \begin{bmatrix} \dot{\boldsymbol{G}} \\ \boldsymbol{\Omega}_{hull} \end{bmatrix} + \sum_{i=1}^{4} \left[\begin{array}{c|c} \mathbb{K}_p^{(i)} & \mathbb{L}_k^{(i)} + \mathbb{C}_p^{R,(i)} \\ \hline \mathbb{C}_p^{R,(i)} & \mathbb{L}_c^{(i)} + \mathbb{W}_p^{G_p,(i)} \end{array} \right] \begin{bmatrix} \dot{\boldsymbol{G}} \\ \boldsymbol{\Omega}_{hull} \end{bmatrix} + \left[\begin{array}{c} \mathbb{C}_p^{R,(i)} \\ \mathbb{W}_p^{G_p,(i)} \end{array} \right] \boldsymbol{\omega}_i$$
$$\underbrace{\phantom{\left[\begin{array}{c|c} \mathbb{K} & \mathbb{C}^G \end{array}\right]}}_{\mathcal{B}_{hull}\ \text{contribution}} \qquad\qquad \underbrace{\phantom{\sum_{i=1}^{4}}}_{\mathcal{B}_{Pi}\ \text{contribution}}$$

$$+ \hat{e} \left[\begin{array}{c|c} \mathbb{0} & \mathbb{0} \\ \hline \mathbb{M}_1^{(i)} & \mathbb{M}_2^{(i)} \end{array} \right] \begin{bmatrix} \dot{\boldsymbol{G}} \\ \boldsymbol{\Omega}_{hull} \end{bmatrix} + \hat{e} \begin{bmatrix} \mathbb{0} \\ \mathbb{N}^{(i)} \end{bmatrix} \boldsymbol{\omega}_i = \begin{bmatrix} \mathbf{0} \\ \mathbf{0} \end{bmatrix} \tag{3.44}$$
$$\underbrace{\phantom{+ \hat{e} \left[\begin{array}{c|c} \mathbb{0} & \mathbb{0} \end{array}\right]}}_{\textit{eccentricity}\ \text{torque only contribution}}$$

which show the three different contributions to the system dynamics.

3.3.1 Constrained dynamics

In this section a simplification of the earlier dynamic model is presented, in order to get a feedback on its validity, it is compared with the model proposed by DeSimone et al. in [22], where a microrobot with one coaxial propeller is designed. The simplification consists in a reduction from six degrees of freedom to two due to the application of constraints to the motion along $\hat{e}_1$ and $\hat{e}_2$ axes; leading the microswimmer to translate and rotate only along $\hat{e}_3$ axis. The aforementioned hypothesis simplifies a lot (3.44) enabling to find the two scalar unknowns $\Omega_{hull,3}$ and $\dot{G}_3$ without numerical computation. We proceed by writing the equations of motion with respect to the third component

$$\begin{cases} (\mathbf{F})_3 = (\mathbf{f}_{hull})_3 + \sum_{i=1}^{4}(\mathbf{f}^{(i)})_3 = 0 \\ (\mathbf{N})_3 = (\boldsymbol{\tau}_{hull})_3 + \sum_{i=1}^{4}(\boldsymbol{\tau}^{(i)} + \mathbf{b}^{(i)})_3 = 0 \end{cases} \tag{3.45}$$

this can be expanded as done in the previous section

$$\begin{bmatrix} 0 \\ 0 \end{bmatrix} = \begin{bmatrix} K_{33} & 0 \\ 0 & W_{33} \end{bmatrix} \begin{bmatrix} \dot{G}_3 \\ \Omega_{h,3} \end{bmatrix} + \sum_{i=1}^{4} \begin{bmatrix} K_{p,33}^{(i)} & L_{k,33}^{(i)} + C_{p,33}^{R,(i)} \\ C_{p,33}^{R,(i)} & L_{c,33}^{(i)} + W_{p,33}^{(i)} \end{bmatrix} \begin{bmatrix} \dot{G}_3 \\ \Omega_{h,3} \end{bmatrix} + \sum_{i=1}^{4} \begin{bmatrix} C_{p,33}^{R,(i)} \\ W_{p,33}^{(i)} \end{bmatrix} \omega_{i,3}$$

$$+ \sum_{i=1}^{4} \begin{bmatrix} 0 & 0 \\ M_{1,33}^{(i)} & M_{2,33}^{(i)} \end{bmatrix} \begin{bmatrix} \dot{G}_3 \\ \Omega_{h,3} \end{bmatrix} + \sum_{i=1}^{4} \begin{bmatrix} 0 \\ N_{33}^{(i)} \end{bmatrix} \omega_{i,3} \tag{3.46}$$

The solution of system (3.46) is given by

$$\begin{cases} \dot{G}_3 = \dfrac{\sum_{i=1}^{4} \chi_{33}^{(i)} \Pi_{33}^{(i)} - \sum_{i=1}^{4} C_{p,33}^{R,(i)} S_{33}^{(i)} - W_{33} \sum_{i=1}^{4} C_{p,33}^{R,(i)}}{T_{33}^{(i)}(W_{33} + \sum_{i=1}^{4} S_{c,33}^{(i)}) - \sum_{i=1}^{4} \chi_{33}^{(i)} \Gamma_{33}^{(i)}} \sum_{i=1}^{4} \omega_{i,3} \\[4mm] \Omega_{h,3} = \dfrac{\sum_{i=1}^{4} T_{33}^{(i)} \Pi_{33}^{(i)} - \sum_{i=1}^{4} C_{p,33}^{R,(i)} \Gamma_{33}^{(i)}}{-T_{33}^{(i)}(W_{33} + \sum_{i=1}^{4} S_{c,33}^{(i)}) + \sum_{i=1}^{4} \chi_{33}^{(i)} \Gamma_{33}^{(i)}} \sum_{i=1}^{4} \omega_{i,3} \end{cases} \tag{3.47}$$

where the below rearrangement of the terms is necessary due to the length of the formula:

$$\chi_{33}^{(i)} = L_{k,33}^{(i)} + C^{R,(i)}, \ \Pi_{33}^{(i)} = W_{p,33}^{(i)} + N_{33}^{(i)},$$

$$S_{33}^{(i)} = L_{k,33}^{(i)} + W_{p,33}^{(i)} + M_{1,33}^{(i)} + M_{2,33}^{(i)},$$

$$T_{33}^{(i)} = K_{33} + \sum_{i=1}^{4} K_{p,33}^{(i)},$$

$$S_{c,33}^{(i)} = L_{c,33}^{(i)} + W_{p,33}^{(i)} + M_{1,33}^{(i)} + M_{2,33}^{(i)},$$

$$\Gamma_{33}^{(i)} = C_{p,33}^{R,(i)} + M_{1,33}^{(i)}.$$

It is stressed that if we set to zero all the arms $\mathbf{r}^{(i)}$ the second line of (3.46) and the coefficients $L_k^{(i)}, L_c^{(i)}$ disappear, then the equation becomes similar to that obtained in [22] for microswimmer with only one coaxial helice.

$$\begin{bmatrix} 0 \\ 0 \end{bmatrix} = \begin{bmatrix} K_{33} & 0 \\ 0 & W_{33} \end{bmatrix} \begin{bmatrix} \dot{G}_3 \\ \Omega_{h,3} \end{bmatrix} + \sum_{i=1}^{4} \begin{bmatrix} K_{p,33}^{(i)} & C_{p,33}^{R,(i)} \\ C_{p,33}^{R,(i)} & W_{p,33}^{(i)} \end{bmatrix} \begin{bmatrix} \dot{G}_3 \\ \Omega_{h,3} \end{bmatrix} + \sum_{i=1}^{4} \begin{bmatrix} C_{p,33}^{R,(i)} \\ W_{p,33}^{(i)} \end{bmatrix} \omega_{i,3} \qquad (3.48)$$

the first term represents the contribution of $\mathcal{B}_{hull}$ in terms of translational and rotational velocities of the hull, the second is the supplement to the translational motion of the body due to the propellers and the last one refers to them but consists in their rotational contribution due to angular velocity $\boldsymbol{\omega}_i$. The solution of system (3.48) is given by

$$\begin{cases} \dot{G}_3 = -\dfrac{W_{33} \sum_{i=1}^{4} C_{p,33}^{R,(i)}}{(K_{33} + \sum_{i=1}^{4} K_{p,33}^{(i)})(W_{33} + \sum_{i=1}^{4} W_{p,33}^{(i)}) - \sum_{i=1}^{4} C_{p,33}^{R,2,(i)}} \sum_{i=1}^{4} \omega_{i,3} \\ \Omega_{h,3} = \dfrac{(K_{33} + \sum_{i=1}^{4} K_{p,33}^{(i)}) \sum_{i=1}^{4} W_{p,33}^{(i)} - \sum_{i=1}^{4} C_{p,33}^{R,2,(i)}}{-(K_{33} + \sum_{i=1}^{4} K_{p,33}^{(i)})(W_{33} + \sum_{i=1}^{4} W_{p,33}^{(i)}) + \sum_{i=1}^{4} C_{p,33}^{R,2,(i)}} \sum_{i=1}^{4} \omega_{i,3} \end{cases} \qquad (3.49)$$

and a numerical method in order to derive the coefficients of the previous tensor is proposed in the next chapter, remembering that here the additivity approximation was used, i.e. we had sum the resistance coefficients in view of neglecting of interactions hypothesis between the hull and the propellers.

Chapter 4

Numerical methods

To solve (3.44), we first need to determine the coefficients of the matrices of the system itself. For this purpose, we use *FEniCSx*, a widespread open-source computing platform that enables the user to solve partial differential equations by quickly translating scientific models into efficient finite element code [34, 37]. To start off, we developed a FEniCSx script aimed at simulating a Stokesian flow around the head of the microswimmer, and then on the propellers, individually, in view of the additivity assumption. The mathematical model considered in the simulations is the one described by (3.21) and implemented with the mini elements technique.

4.1 Mini-Elements for Stokes problem

The mini finite element was first introduced by Arnold, Brezzi and Fortin, specifically conceived for the discretization of the Stokes problem. Let $\mathcal{T}_h = \{T \in \mathcal{T}_h : T \subset \mathcal{V}/\mathcal{B}\}$ be an admissible family of triangulation on the entire domain and let us define the discrete functional spaces:
$V_h = \{v_h \in C^0(T) : v_h \in P_{1+3} \quad \forall T \in \mathcal{T}_h\}$ and $Q_h = \{q_h \in C^0(T) : q_h \in P_1 \quad \forall T \in \mathcal{T}_h\}$.
It is possible to formulate velocity and pressure functions for the mini-elements as follows
$v_h = v_l + v_b$, where v_l is a piecewise-linear function (P_1) and v_b is a cubic function (P_3);
$q_h = q_l$, where q_l is piecewise-linear function. It is noteworthy that this enrichment to the velocity, due to the "bubble" term v_b, has a stabilization function and is not properly aimed at improving the accuracy of the approximation of the real velocity field v_l. This implementation leads to a stable and convergent approximation of the Stokes problem as demonstrated in [23], with a strong reduction in computational costs.

4.1.1 Code validation

To test our code, we first simulated a flow in free field with longitudinal inlet velocity, directed along the z axis, for two different geometries: a sphere and an ellipsoid. Both geometries can move within the domain, hence our flow field can be written as follows:

$$\mathbf{U}(\mathbf{x}) = \mathbf{u}(\mathbf{x}) + \mathbf{v}(\mathbf{x}) \tag{4.1}$$

where $\mathbf{u}(\mathbf{x})$ describes the velocity field, assumed to be fully known, and which we refer to as background flow; $\mathbf{v}(\mathbf{x})$ is the disturbance flow due to the moving particle which has the following affine structure

$$\mathbf{v}(\mathbf{x}) = \boldsymbol{v}_t + \boldsymbol{\omega} \times \mathbf{r} \tag{4.2}$$

where $\boldsymbol{v}_t = (v_x, v_y, v_z)$, $\boldsymbol{\omega} = (\omega_x, \omega_y, \omega_z)$ are the translational and rotational velocity, respectively.

The table below shows how boundary conditions are imposed in every part of the domain when the background flow is assumed to be zero:

	Inlet velocity	Wall conditions	Outlet pressure	Particle velocity
Case I	$\boldsymbol{v}_t = (0,0,0)$	$\boldsymbol{v}_t = (0,0,0)$ or $p = 0$	0	(-1,0,0) & $\boldsymbol{w} = \mathbf{0}$
Case II	$\boldsymbol{v}_t = (0,0,0)$	$\boldsymbol{v}_t = (0,0,0)$ or $p = 0$	0	(0,-1,0) & $\boldsymbol{w} = \mathbf{0}$
Case III	$\boldsymbol{v}_t = (0,0,0)$	$\boldsymbol{v}_t = (0,0,0)$ or $p = 0$	0	(0,0,-1) & $\boldsymbol{w} = \mathbf{0}$
Case IV	$\boldsymbol{v}_t = (0,0,0)$	$\boldsymbol{v}_t = (0,0,0)$ or $p = 0$	0	$\boldsymbol{v}_t = \mathbf{0}$ & $\boldsymbol{w}_x \times \mathbf{r}$
Case V	$\boldsymbol{v}_t = (0,0,0)$	$\boldsymbol{v}_t = (0,0,0)$ or $p = 0$	0	$\boldsymbol{v}_t = \mathbf{0}$ & $\boldsymbol{w}_y \times \mathbf{r}$
Case VI	$\boldsymbol{v}_t = (0,0,0)$	$\boldsymbol{v}_t = (0,0,0)$ or $p = 0$	0	$\boldsymbol{v}_t = \mathbf{0}$ & $\boldsymbol{w}_z \times \mathbf{r}$

Table 4.1: Boundary conditions: linear and angular velocities are expressed in [m/s] and [1/s], respectively. Pressure is specified in [Pa]

In order to obtain all velocity fields we have to perform six simulations by referring to the parameters in table 4.1 above, one for each axis direction and each velocity condition. It is important to note that the boundary conditions on the wall were first set with zero velocity and then with zero pressure. This procedure aims to numerically calculate the resistance coefficients and compare them with known values from literature. It is important to point out that the values which we refer to are calculated in zero flow conditions throughout the whole domain, in fact the main aim of the simulation is to make sure that the presence of the computational domain does not significantly affect the accuracy of the numerical prediction of viscous forces and torques on the swimmer.

In view of simulating a free flow without the disturbance induced by the boundaries, a ratio $R/r = 80$ is adopted, where $R = 4 \cdot 10^3$ mm, $r = 50$ mm are the radii of the cylinder and the sphere, respectively. The dimensions of the ellipsoid are $a_1 = a_2 = 50$ mm and the longitudinal semi-axis along $\hat{e}_3$ measures $a_3 = 150$ mm.
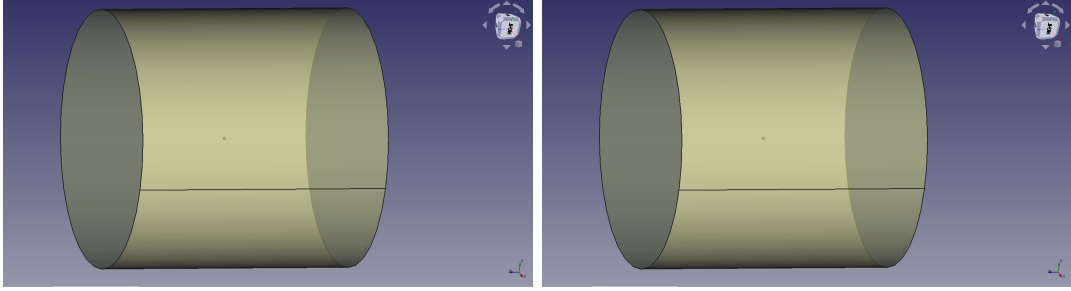

Figure 4.1: Validation domain - Sphere & Ellipsoid

The mesh consists of tetrahedral elements with a much better refinement around the area adjacent to the particle, in order to better capture the phenomenology in this region, see figure 4.2. In order to choose an appropriate mesh for the simulations a quick study on the
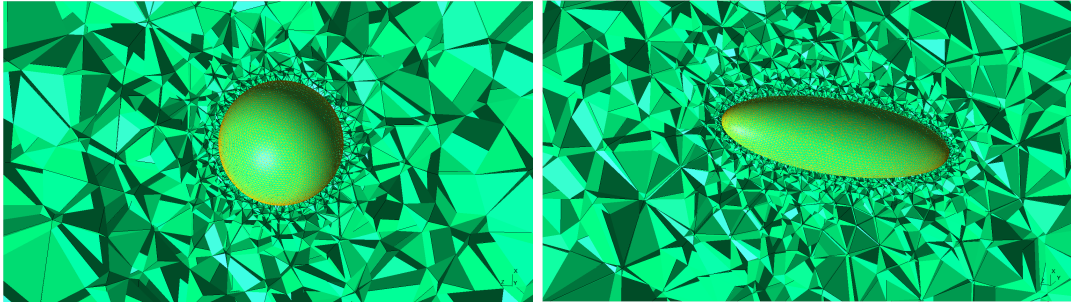
Figure 4.2: Mesh refinement around the particle

influence of the number of elements is performed on both geometries. The quality check of the mesh is possible thanks to the interface of GMSH which provides three parameters and the intervals in which they must lie in order to evaluate its goodness. This procedure is important in order to obtain a reliable simulation, but it is out of scope for this work, hence we do not study the influence of these parameters and limit the analysis to the number of elements. Figure 4.5 shows the comparison between analytical and numerical results with respect to this number. This analysis, performed on both geometries, gives for the ellipsoid the best outcome with a finer mesh, while, with regard to the sphere, the simulations give optimal results for the translational coefficients using a coarser mesh, whereas for the rotational coefficients a good approximation is obtained with a finer mesh instead.
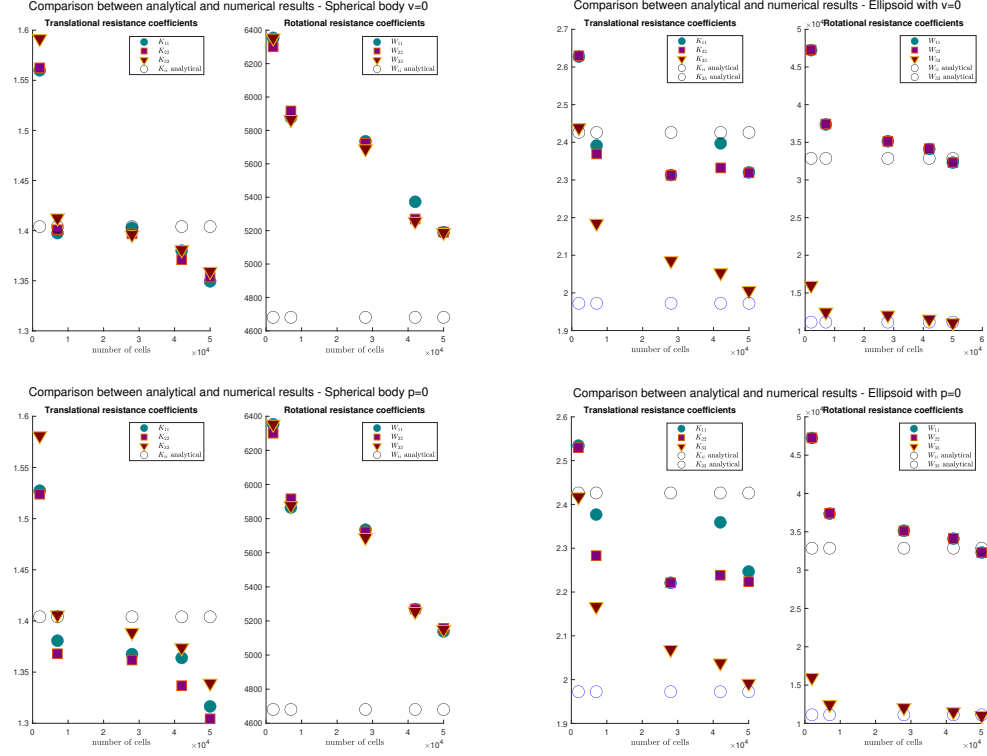
Figure 4.3: Convergence vs num of elements for the two different wall boundary conditions

The analytical coefficients are calculated from the formulae below, as exploited in [16], where $\epsilon = \sqrt{1 - \dfrac{a_1}{a_3}}$ and the superscripts "s" and "e" stand for sphere and ellipsoid, respectively.

$$
\begin{cases}
K_{ii}^s = 6\pi\mu r \quad \forall i = 1, 2, 3 \\
W_{ii}^s = 8\pi\mu r^3 \quad \forall i = 1, 2, 3 \\
K_{ii}^e = 6\pi\mu a_3 \dfrac{16}{3}\epsilon^3 \left[2\epsilon + (3\epsilon^2 - 1)log\Big(\dfrac{1+\epsilon}{1-\epsilon}\Big) \right]^{-1} \quad \forall i = 1, 2 \\
K_{33}^e = 6\pi\mu a_3 \dfrac{8}{3}\epsilon^3 \left[-2\epsilon + (\epsilon^2 + 1)log\Big(\dfrac{1+\epsilon}{1-\epsilon}\Big) \right]^{-1} \\
W_{ii}^e = 8\pi\mu a_3^3 \dfrac{4}{3}\epsilon^3(2 - \epsilon^2) \left[-2\epsilon + (1 + \epsilon^2)log\Big(\dfrac{1+\epsilon}{1-\epsilon}\Big) \right]^{-1} \quad \forall i = 1, 2 \\
W_{33}^e = 8\pi\mu a_3^3 \dfrac{4}{3}\epsilon^3(1 - \epsilon^2) \left[2\epsilon - (1 - \epsilon^2)log\Big(\dfrac{1+\epsilon}{1-\epsilon}\Big) \right]^{-1}
\end{cases}
\tag{4.3}
$$

Table 4.4 contains the coefficients and the relative error with respect to the analytical data in the case of a 50′000 elements mesh, for both the cases of null velocity (third column) and null pressure (last column) on the wall domain.

	Analytical	Numerical	Error L$_1$	Numerical	Error L$_1$
K_{11}^s	1.404029	1.3494	0.0389	1.316514	0.0623
K_{22}^s	1.404029	1.3537	0.0358	1.304382	0.0710
K_{33}^s	1.404029	1.3593	0.0319	1.339157	0.0462
W_{11}^s	4680.97	5190.05	0.1088	5138.41	0.0977
W_{22}^s	4680.97	5191.36	0.1090	5156.52	0.1016
W_{33}^s	4680.97	5188.52	0.1084	5150.36	0.1003
K_{11}^e	2.42616	2.32016	0.0437	2.24684	0.0739
K_{22}^e	2.42616	2.31902	0.0442	2.22362	0.0835
K_{33}^e	1.97237	2.00600	0.0171	1.99163	0.0098
W_{11}^e	32873.3	32298.83	0.0175	32296.25	0.0176
W_{22}^e	32873.3	32300.51	0.0174	32297.26	0.0175
W_{33}^e	10505.5	11026.29	0.0468	12054.58	0.0464

Table 4.2: Resistance coefficients, units: K [kg/s], W [kg·mm^2/s] the first numerical result refers to null velocity condition at the walls while the second to null pressure

From a numerical point of view, the coupling coefficients, which correspond to the entries of the tensor $\mathbb{C}^R$, are less than the other entries, in fact the maximum value reached is $C_{15} = 1.17[kg \cdot mm/s]$. This can be attributed to a use of a quite coarse mesh, because of the large computational cost of simulations, so we will have to return to this aspect in the future to clarify this numerical limit. Note that this aspect will affect the calculation of trajectories. In the following pages the velocity streamlines and pressure contours are shown (see figures (4.4), (4.5) and (4.6)). These plots provide further confirmation that the simulations returns sensible values. Moreover, several works are readily available in literature for both a spherical shape and an ellipsoidal one, where typical velocity streamlines and pressure contours are examined [38, 39]. By comparing these works with our results, we found strong correspondences as far as the results shown are concerned. The left side of figures 4.4, 4.5, 4.6 and 4.7 is relative to the sphere, while on the right we have the results for the ellipsoid. Both cases refer to the free flow domain and for the standard case flow past a sphere, with unitary inlet velocity only along $z-$axis i.e. $(0, 0, 1)$.
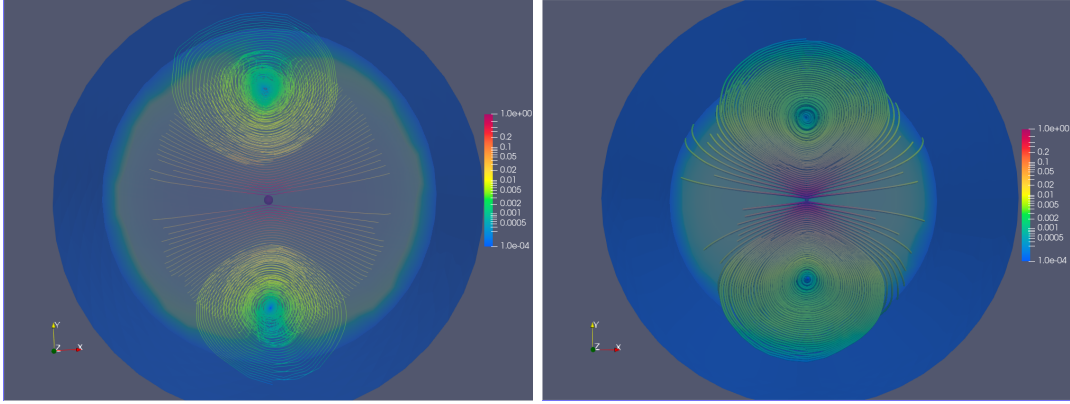
Figure 4.4: Normalized velocity streamlines - translation along x
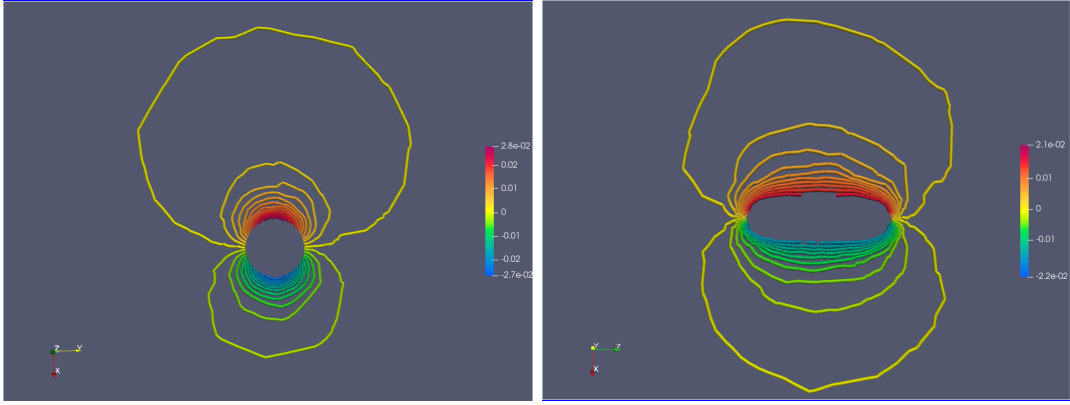

Figure 4.5: Pressure contours - translation along x

In reference to the free flow condition with zero velocity everywhere, the streamlines have the typical pattern with recirculating regions, on the other hand when a null pressure is imposed at the wall no recirculation occurs. For what concerns the pressure contours they qualitatively found confirmation in literature. Also in a quantitative way we guess a lower pressure in the ellipsoid rather than the sphere due to its wider section.

Finally, figure (4.7) depicts the typical benchmark case, in which the no-slip condition is applied on the particle, here, the streamlines around it match what we expect from the theory. The first thing to note is that for these very small Reynolds numbers the pattern of the flow is symmetrical front to back.

However, better results in terms of agreement between numerical and analytical results, i.e. the maximum error was significantly reduced, were achieved by simulating with a mesh made up of about $350'000$ cells.

Because of the expensive computational cost in terms of simulation time, this arrangement was initially excluded, and a coarser mesh was preferred instead. For completeness, in table
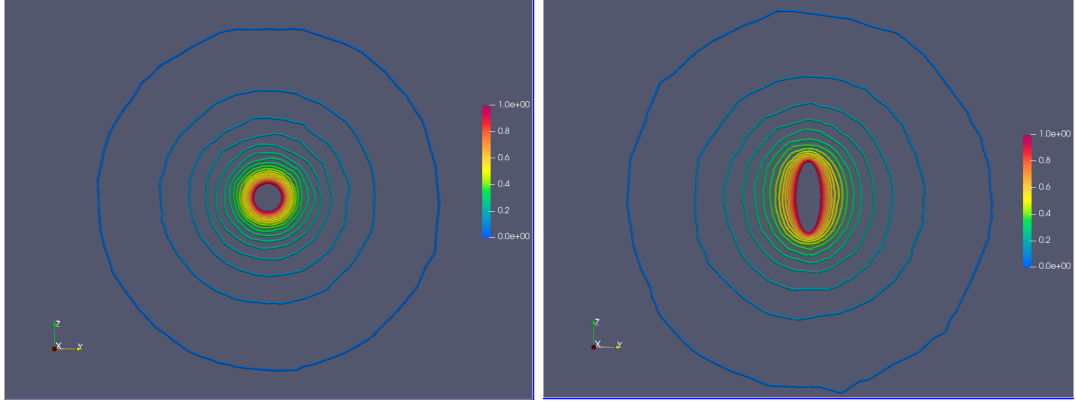
Figure 4.6: Normalized velocity contours - translation along x
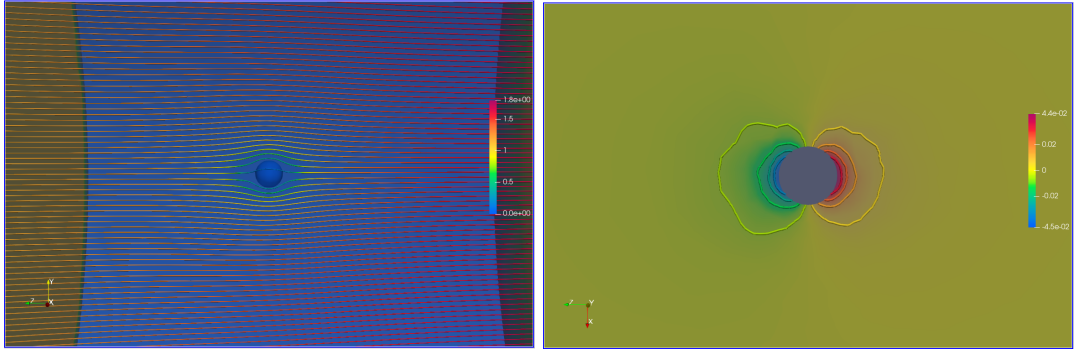
Figure 4.7: Velocity streamlines & pressure contours - no-slip condition

(4.3) we report the results obtained with the finer mesh only for the ellipsoidal shape.

	Analytical	Numerical	Error
K_{11}^e	2.42616	2.4317	0.0023
K_{22}^e	2.42616	2.4282	$8 \cdot 10^{-4}$
K_{33}^e	1.97237	2.0246	0.0265
W_{11}^e	32873.3	32360.03	0.0162
W_{22}^e	32873.3	32342.20	0.0174
W_{33}^e	10505.5	10727.87	0.02

Table 4.3: Resistance coefficients, for the ellipsoid with fine mesh with 350'000 elements

4.1.2 Propeller coefficients computation

In this section we report an experimental study of the flow field and the computations of the propeller hydrodynamic resistance coefficients. First of all we are interested in understanding how propulsion can arise using such a type of propeller. An interesting and useful result which states that a rod dragged along its axis at velocity $\boldsymbol{v}$ feels a resisting force proportional to $-\boldsymbol{v}$, that is also directed along the axis.
A rod dragged perpendicular to its axis feels a resistive force also proportional to $-\boldsymbol{v}$, that is, directed perpendicular to the axis, but with a larger constant of proportionality [29]. This concept is clarified in a simple manner by the illustration (4.8):
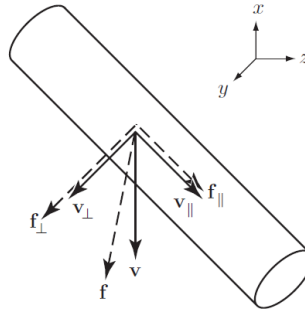
Figure 4.8: Forces acting on a moving rod at low Reynolds, figure taken by [29]

In 1973, H. Berg and R. Anderson argued that bacteria cranked their flagellum at its base in a rigid rotary motion leading to a propulsive force which pulls (or pushes) their body in a certain direction. Substantially, the direction of the motion is an information coming a priori from the propeller chirality. Mathematically, changing the chirality leads to a change in the sign of the so-called coupling tensor $\mathbb{C}$, which is different from zero for our geometry due to the fact that the net drag force is not anti-parallel to $\mathbf{v}$. In order to compute the coefficients of matrix $\mathbb{C}$ for a helical propeller, which is not an easy task for complex geometries such as this one, we develop a program and then compare the generated flow fields with the ones obtained in [30]. We perform the simulation over both left and right-handed helix with length 200mm, pitch 53mm and radius 8.5mm. The rotational velocity is set to a constant value and the computational domain is large enough for the free flow approximation to be valid, as did in the validation section. A fine mesh with roughly $350'000$ elements is adopted.
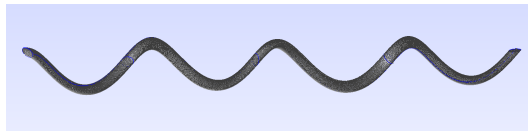

Figure 4.9: Helix mesh representation in GMSH

The coefficients are extrapolated from the knowledge of the fluid field solutions through the formula below, as reported in [22]:

$$K_{i,j} = \int_{\mathcal{V}} D\mathbf{u}_i \cdot D\mathbf{u}_j \, d\mathbf{x} \tag{4.4}$$

where the subscript i, j are representative for the i, j-th experiments and vary from one to six while the operator D stands for the symmetric part of the gradient. More explicitly, we can write the coefficients as follows:

$$\begin{cases} K_{i,i} = \int_{\mathcal{V}} D\mathbf{u}_i \cdot D\mathbf{u}_i \, d\mathbf{x} & \forall i = 1, 2, 3 \\ W_{j,j} = \int_{\mathcal{V}} D\mathbf{u}_j \cdot D\mathbf{u}_j \, d\mathbf{x} & \forall j = 4, 5, 6 \\ C_{i,j} = \int_{\mathcal{V}} D\mathbf{u}_i \cdot D\mathbf{u}_j \, d\mathbf{x} \end{cases} \tag{4.5}$$

highlighting the three different resistive contributions to the motion: translational, rotational and coupling. The matrices below contain the numerical values of this coefficients, expressed in $[kg/s]$, $[kg \cdot mm^2/s]$ and $[kg \cdot mm/s]$ for the cases in which the propeller rotates clockwise and is a left-handed rigid helix (4.6) or a right-handed (4.7):

$$\left[\begin{array}{c|c} K_p & C_p^T \\ \hline C_p & W_p \end{array} \right] = \begin{bmatrix} 0.8471 & 0.0026 & 0.0043 & -0.24 & -10.51 & 0.21 \\ 0.0026 & 0.8475 & -0.0048 & 10.08 & -0.3729 & 0.2685 \\ 0.0043 & -0.0048 & 0.7483 & 0.34 & -0.7545 & 0.6887 \\ -0.24 & 10.08 & 0.34 & 4798.98 & 6.0257 & 84.15 \\ -10.51 & -0.3729 & -0.75 & 6.02 & 4784.29 & 138.04 \\ 0.21 & -0.75 & 0.6887 & 84.15 & 138.04 & 178.82 \end{bmatrix}. \tag{4.6}$$

$$\left[\begin{array}{c|c} K_p & C_p^T \\ \hline C_p & W_p \end{array} \right] = \begin{bmatrix} 0.82222 & 0.0021 & 0.0024 & 0.2958 & -8.1475 & -0.0749 \\ 0.0021 & 0.82222 & 0.0058 & 8.4475 & 0.3364 & 0.1592 \\ 0.0024 & 0.0058 & 0.7250 & -0.2595 & -0.7023 & -0.6924 \\ 0.2958 & 8.4475 & -0.2595 & 4538.20 & -29.43 & 69.45 \\ -8.1475 & 0.3364 & -0.7023 & -29.43 & 4485.53 & 131.77 \\ -0.0749 & 0.1592 & -0.6924 & 69.45 & 131.77 & 173.37 \end{bmatrix}. \tag{4.7}$$

The structure of the matrix displays some symmetry properties, as expected, and the sign of the elements depends on the direction of the angular velocity. We want to investigate the flow behaviour in order to qualitatively compare the two type of propellers. In the next page our results are shown choosing the XZ as sectioning plane.
Figure (4.10) shows the streamlines near a left-handed propeller when it rotates in free-flow condition. They tangle around it, as expected when an object rotates within a viscous fluid.
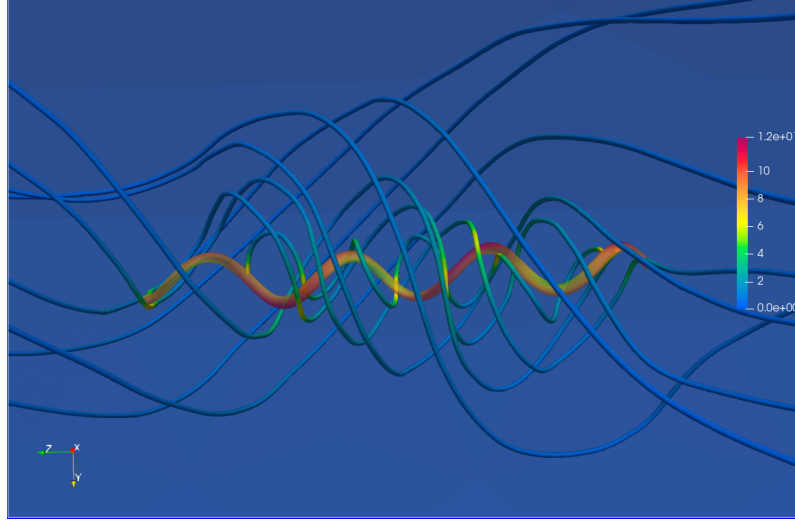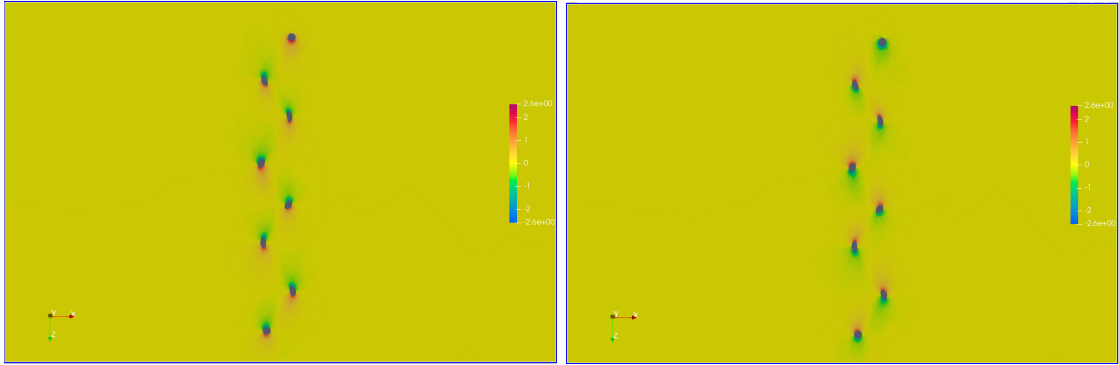
Figure 4.10: Velocity streamlines

Figure 4.11: Pressure contours $[MPa]$

In (4.11) the pressure contours are shown, in both cases of anti-clockwise and clock-wise direction of angular velocity, highlighting how high and low pressure areas, rightly, alternate as described in [31]. In figure (4.12) the axial velocity, i.e. the z component, is shown, demonstrating the downward and upward motion of the fluid as [32] proposes.

In order to have a full comparison with this last article we add to (4.12) other two results, depicted in (4.17) and (4.14) which illustrate the transverse velocity of the flow, along x-axis and the vector field around the helix, in anti-clockwise and clockwise cases.

The directions of the arrows in the two cases are graphically the same, but from the legend it is clear that one has a positive sign and the other is negative. Hence, it can be concluded that the motion occurs in opposite directions, as rightly predicted by the theory, see [33].

29
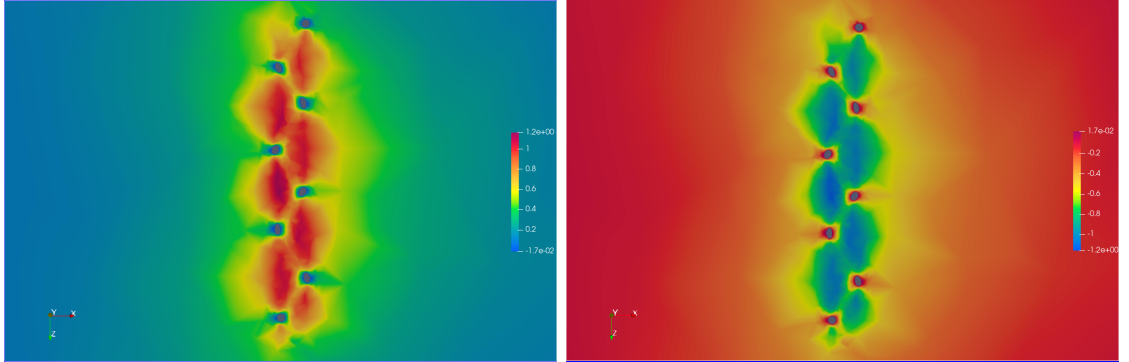
Figure 4.12: z component of velocity $[mm/s]$
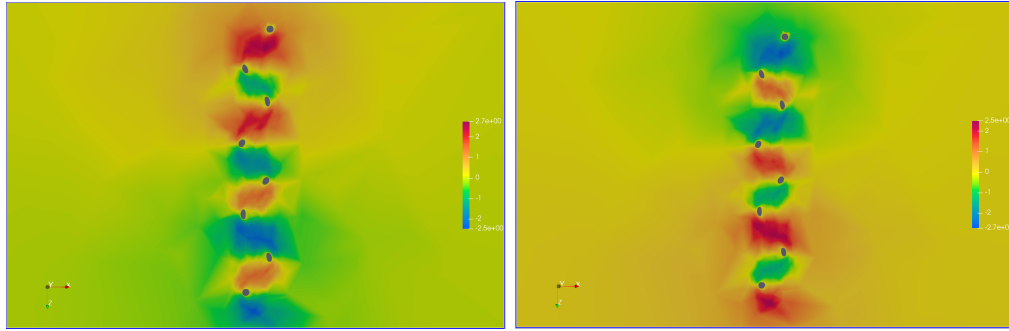
Figure 4.13: x component of the velocity $[mm/s]$

In the table below, we compare our numerical results, in terms of velocity and pressure, with those obtained by [31], where a similar simulation has been performed.

	Siva Kumar et al	Thesis
ω	1.57 rad/s	1 rad/s
$\mathbf{r}$	$22.7 \cdot 10^{-3}$ m	$8.5 \cdot 10^{-3}$ m
L	$200 \cdot 10^{-3}$ m	$220 \cdot 10^{-3}$ m
λ	66 mm	53 mm
$v_{z,max}$	0.0127 m/s	0.0012 m/s
p_{max}	0.1 MPa	2.1 MPa

Table 4.4: Numerical comparison. ω is the angular velocity, $\mathbf{r}$, L, λ are the helix radius, the length and the pitch, respectively.
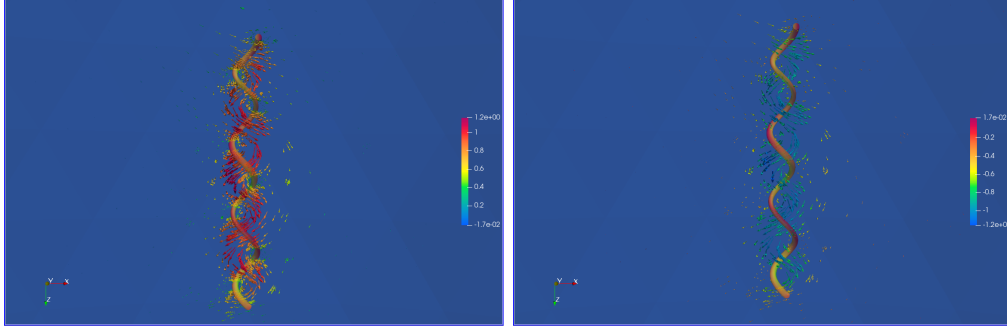
Figure 4.14: Velocity vector field $[mm/s]$

Finally, the influence of the chirality of the propellers has been studied. For this purpose, a right-handed helix was built with the same parameters used in the previous model, and the same simulations were performed. What emerges is that changing the chirality alters the direction of the speed and, therefore, also the resulting thrust will induce a motion in the opposite direction. This is also reflected in the coefficients of the resistance matrix, which are very close to those of the left-handed helix but with opposite sign.
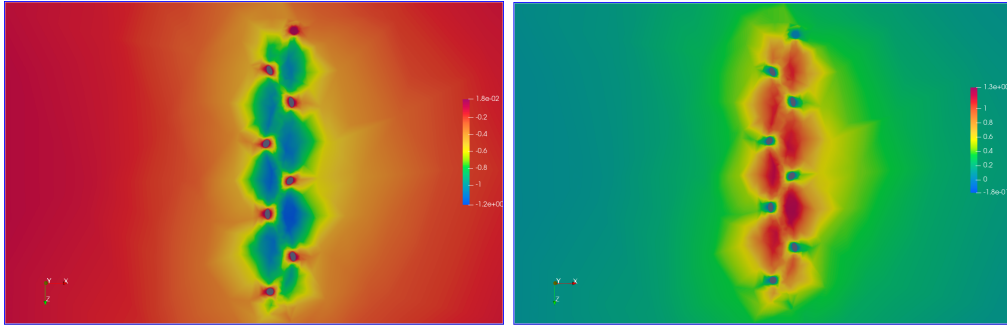
Figure 4.15: z component of the velocity $[mm/s]$

Note that we have presented both the cases of anti-clockwise and clockwise rotation. The velocity fields obtained are opposite to each other, hence if we consider two propellers with the same chirality which rotates in opposite direction the total sum of the thrust is zero.
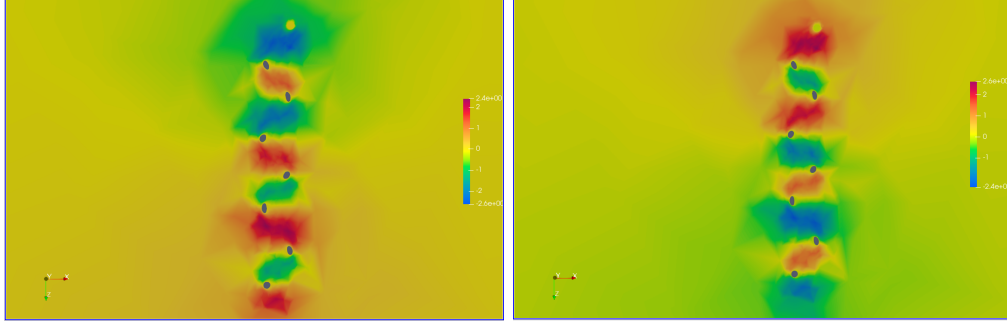
Figure 4.16: x component of the velocity $[mm/s]$

4.1.3 Hull coefficients computation

As already described in the main introduction, the hull is the head of the microswimmer. Below, for thoroughness, we report its mesh as previously done for the helix:
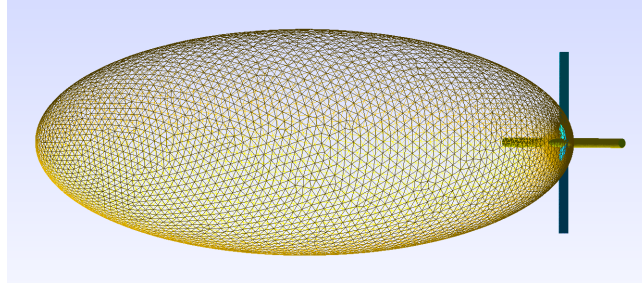

Figure 4.17: mesh details for the hull body

$$\left[\begin{array}{c|c} K & C^T \\ \hline C & W \end{array}\right] = \begin{bmatrix} 2.3795 & 0.0283 & 0.0063 & 1.4093 & 17.27 & 0.0836 \\ 0.0283 & 2.3885 & 0.0020 & -12.95 & 1.063 & 0.3433 \\ 0.0063 & 0.00204 & 2.0421 & -0.1791 & 0.547 & -0.0272 \\ 1.4093 & -12.95 & -0.1791 & 35283.06 & 54.08 & 3.2939 \\ 17.27 & 1.0633 & 0.547 & 54.08 & 35398.22 & 17.01 \\ 0.0836 & 0.3433 & -0.027 & 3.293 & 17.01 & 11246.48 \end{bmatrix}. \quad (4.8)$$

Again, we expect to find a symmetric matrix whose diagonal elements are very close to those of the ellipsoid, but different from zero elsewhere, albeit always small with respect to the rotational ones. Now, we have all the elements to solve (3.44) and compute the velocities of the micro-robot $\dot{\mathbf{G}}$, $\mathbf{\Omega}_{hull}$. In figure 4.18 below, a qualitative view of what happens in terms of streamlines during a translational and a rotational motion, both along the z axis, is shown:
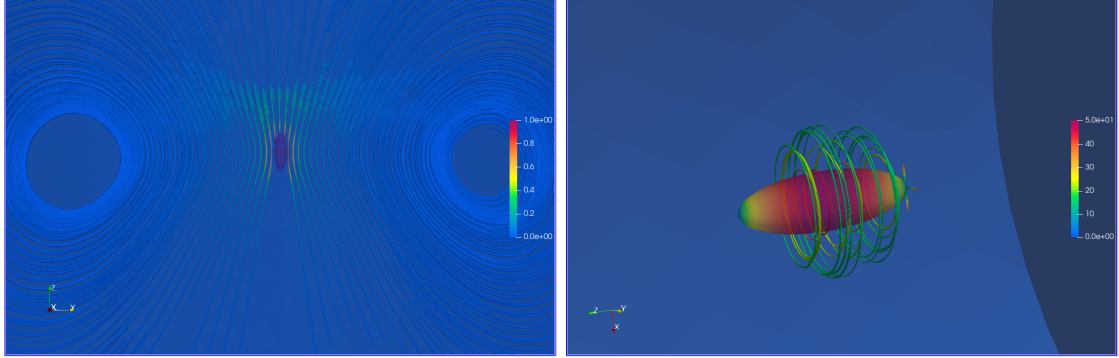
Figure 4.18: Streamlines for translational (left) and rotational velocity along the z-axis (right)

In order to better investigate the pressure acting on the body, we propose the graphical visualization of the contours:
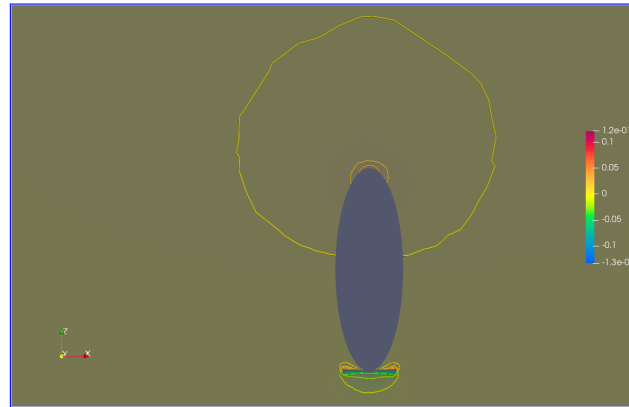

Figure 4.19: Pressure contours $[MPa]$

Basically, from the point of view of the fields $\mathbf{u}(\mathbf{x})$ and $p(\mathbf{x})$, the results are very similar to those obtained for the ellipsoid, as expected.

Chapter 5

Propellers configurations

The last chapter of this thesis aims to solve the equations of dynamics in order to derive the values of the unknowns (the linear and angular velocities of the microswimmer) for different geometrical configurations and velocities of the propellers. We have seen and demonstrated how the angular velocities and chirality of the propellers affect the motion of the body by modifying the fluid field around them and thus inducing a thrust. Now, we want to investigate how this information can be used to reduce wobbling. *Python* has been used to solve the dynamics, in particular the numerical libraries *NumPy* and *SciPy* were used to assemble the matrices and solve the compact form of system (3.44), defined as

$$\mathbf{F} = \mathcal{R}\mathbf{U} + \mathbf{b} \tag{5.1}$$

where $\mathbf{F} \in \mathbb{R}^{6,1}$ is the vector of the generalized forces which incorporates the three forces and the three moments, assumed to be zero as previously described, $\mathcal{R} \in \mathbb{R}^{6,6}$ is the grand resistance matrix composed by the sum of all resistance matrices for each body part, and $\mathbf{U} \in \mathbb{R}^{6,1}$ is the unknown term whose the first three components represent the translational velocities and the last three stand for the angular ones. The vector $\mathbf{b} \in \mathbb{R}^{6,1}$ is built using the propellers angular velocities. We have considered two different directions for the propeller angular velocity, that is

$$\begin{cases} \boldsymbol{\omega} = [0,0,+1]^T & \text{for clockwise direction} \\ \boldsymbol{\omega} = [0,0,-1]^T & \text{for anti-clockwise direction} \end{cases} \tag{5.2}$$

The units of $\boldsymbol{\omega}$ are $[rad/s]$. All the velocities values presented in the following pages are normalized with respect to the body length $R_h = 150\,mm$ and angular frequency $f = \dfrac{\omega}{2\pi}\,Hz$.

The micro-robot velocities are expressed in the body frame, whose basis is composed by the time independent unit vectors $\{\hat{e}'_1, \hat{e}'_2, \hat{e}'_3\}$. The laboratory frame on the other hand has as basis the time dependent unit vectors $\{\hat{e}_1(t), \hat{e}_2(t), \hat{e}_3(t)\}$. The following relations hold:

$$\begin{cases} \dot{\hat{e}}_i = \mathbf{\Omega}_{hull} \times \hat{e}'_i, & i = 1, 2, 3 \\ \dot{\mathbf{G}} = \sum_{i=1}^{3} v_i \hat{e}'_i, & i = 1, 2, 3 \end{cases} \tag{5.3}$$

The axial vector $\mathbf{\Omega}_{hull} = [\Omega_1, \Omega_2, \Omega_3]$ can be associated to the skew matrix

$$\mathbb{A} = \begin{bmatrix} 0 & -\Omega_3 & \Omega_2 \\ \Omega_3 & 0 & -\Omega_1 \\ -\Omega_2 & \Omega_1 & 0 \end{bmatrix} \tag{5.4}$$

that allow us to write the first equation in (5.3) as

$$\dot{\hat{e}}_i = \mathbb{A}\hat{e}'_i \tag{5.5}$$

The solution of this equation is given by

$$\hat{e}_i(t) = \mathbb{M}(t)\hat{e}'_i \tag{5.6}$$

where the exponential matrix $\mathbb{M}(t) = \exp(\mathbb{A}t)$ is defined.
If we assume the body frame is coincident with the laboratory frame at $t = 0$ [40], we get

$$\hat{e}_1(t) = \frac{1}{\Omega^2} \begin{bmatrix} \Omega_1^2 + (\Omega_2^2 + \Omega_3^2)cos\Omega t \\ \Omega_1\Omega_2(1 - cos\Omega t) + \Omega_3\Omega sin\Omega t \\ \Omega_1\Omega_3(1 - cos\Omega t) - \Omega_2\Omega sin\Omega t \end{bmatrix} \tag{5.7}$$

$$\hat{e}_2(t) = \frac{1}{\Omega^2} \begin{bmatrix} \Omega_1\Omega_2(1 - cos\Omega t) + \Omega_3\Omega sin\Omega t \\ \Omega_2^2 + (\Omega_1^2 + \Omega_3^2)cos\Omega t \\ \Omega_2\Omega_3(1 - cos\Omega t) - \Omega_1\Omega sin\Omega t \end{bmatrix} \tag{5.8}$$

$$\hat{e}_3(t) = \frac{1}{\Omega^2} \begin{bmatrix} \Omega_1\Omega_3(1 - cos\Omega t) + \Omega_2\Omega sin\Omega t \\ \Omega_2\Omega_3(1 - cos\Omega t) - \Omega_1\Omega sin\Omega t \\ \Omega_3^2 + (\Omega_1^2 + \Omega_2^2)cos\Omega t \end{bmatrix} \tag{5.9}$$

and integrating the second equation in (5.3) we get the position of the center of gravity

$$\mathbf{G}(t) = \dot{G}t cos(\psi)\hat{\Omega} + \frac{\dot{G}}{\Omega_h} sin(\psi)\Big(cos(\Omega_h t)\hat{U} + sin(\Omega_h t)\Big)\hat{W} \tag{5.10}$$

where G, Ω_h are the L_2 norm of the two velocity vectors $\dot{\mathbf{G}}$ and $\mathbf{\Omega}_{hull}$, $arcos(\psi) = \dfrac{\mathbf{G} \cdot \mathbf{\Omega}_{hull}}{G\Omega_h}$ is the inverse cosine of the angle ψ between $\dot{\mathbf{G}}$ and $\mathbf{\Omega}_{hull}$. The triplet $\{\hat{\Omega}, \hat{U}, \hat{W}\}$ is an orthonormal basis.

5.0.1 First experiment

Now, based on the previous qualitative analysis on the flow direction and, consequently, on the thrust direction, which is affected by the different geometry and/or angular velocity orientation, we try to solve the dynamics considering four propellers disposed as shown in the figure 5.1.

Figure 5.1: XY plane for the propulsive system

The first setup, left side of figure 5.1, represents the condition in which the propellers generate a propulsion with the highest values of the velocity components on the *XY* plane. This is due to their different chirality, which allows motion even when the propulsion along the *z*-axis is reduced because of the different directions and magnitudes of the thrusts. This leads to a trajectory characterized by a large radius of curvature, which is not good for our purposes. On the other hand, in the next configuration, the micro-robot does not move, because the propellers with the same chirality (red & blue) rotate in opposite directions and so the thrust are opposite to each other and of equal magnitude. The helicoidal path of the micro-robot is shown below in figure 5.2. The blue line represents the first setup and the red diamond the second one which does not evolve in time.
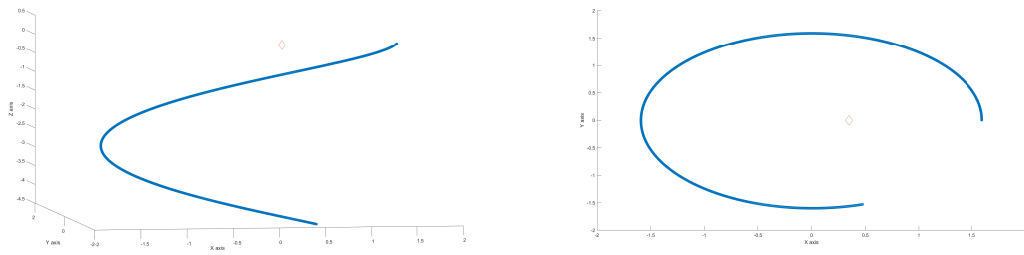

Figure 5.2: First experiment - 3D trajectory (left) and its projection on the *XY* plane (right).

5.0.2 Second experiment

Here, we want to compare two situations: first, the case in which all the propellers rotate anti-clockwise, and have the same chirality, for example right-handed and second when two of four propellers are switched off.

Figure 5.3: XY plane for the propulsive system

The velocities for both cases are here summarized. In figure 5.4 the trajectories are shown. Note that the first micro-robot configuration ensures higher velocity along the direction of motion z, and this is correct since it has two more contributions in terms of thrust with respect to the other case. Furthermore, the fact that two propellers are switched off does not mean that they do not oppose resistance to the motion, indeed the micro-robot follows the same trajectories in both cases, with only different axial velocity. These two configurations are pretty similar and they both reduce the wobbling by one order of magnitude with respect to the first experiment.

$$
\begin{bmatrix}
v_x \\
v_y \\
v_z \\
\Omega_{hull,x} \\
\Omega_{hull,y} \\
\Omega_{hull,z}
\end{bmatrix}
=
\begin{bmatrix}
7.5 \cdot 10^{-4} \\
-1.3 \cdot 10^{-3} \\
3.5 \cdot 10^{-3} \\
9 \cdot 10^{-4} \\
1.3 \cdot 10^{-3} \\
9.1 \cdot 10^{-3}
\end{bmatrix}
,
\qquad
\begin{bmatrix}
v_x \\
v_y \\
v_z \\
\Omega_{hull,x} \\
\Omega_{hull,y} \\
\Omega_{hull,z}
\end{bmatrix}
=
\begin{bmatrix}
4 \cdot 10^{-4} \\
-6.4 \cdot 10^{-4} \\
1.7 \cdot 10^{-3} \\
4 \cdot 10^{-4} \\
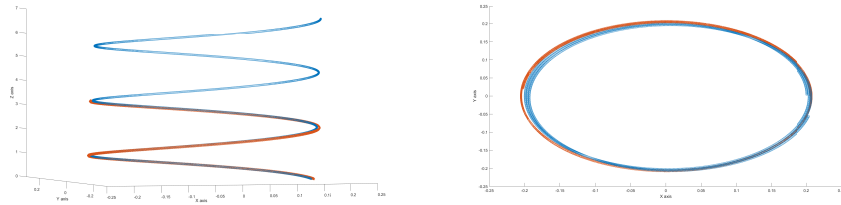7.4 \cdot 10^{-4} \\
4.5 \cdot 10^{-3}
\end{bmatrix}
\tag{5.11}
$$

Figure 5.4: Second experiment - 3D trajectory (left) and its projection on the XY plane (right).

5.0.3 Third experiment

In the third experiment we investigate the effects of a propeller rotating in the opposite direction to all the others, whether it possesses the same chirality (left), or it does not(right).
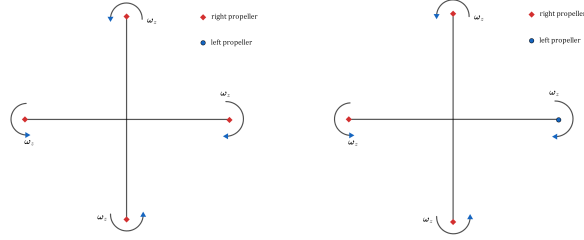

Figure 5.5: XY plane for the propulsive system

It is evident that when the chirality of the propeller is changed, wobbling worsens resulting in a wider trajectory depicted in red in figure 5.6. We can also check this behaviour numerically from the vectors looking at the order of magnitude of the XY velocities:

$$
\begin{bmatrix} v_x \\ v_y \\ v_z \\ \Omega_{hull,x} \\ \Omega_{hull,y} \\ \Omega_{hull,z} \end{bmatrix} = \begin{bmatrix} 3.7 \cdot 10^{-4} \\ -6.6 \cdot 10^{-4} \\ 1.7 \cdot 10^{-3} \\ 4.5 \cdot 10^{-4} \\ 6.6 \cdot 10^{-4} \\ 4.5 \cdot 10^{-3} \end{bmatrix}, \quad \begin{bmatrix} v_x \\ v_y \\ v_z \\ \Omega_{hull,x} \\ \Omega_{hull,y} \\ \Omega_{hull,z} \end{bmatrix} = \begin{bmatrix} 1 \cdot 10^{-3} \\ -2.2 \cdot 10^{-3} \\ 1.7 \cdot 10^{-3} \\ 1 \cdot 10^{-3} \\ 1.4 \cdot 10^{-3} \\ 4.5 \cdot 10^{-3} \end{bmatrix} \tag{5.12}
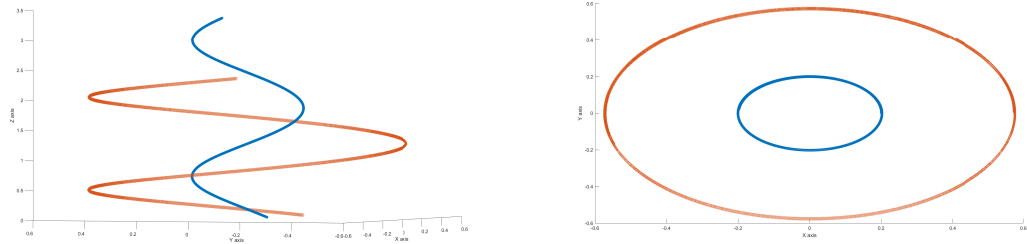$$

Figure 5.6: Third experiment - 3D trajectory (left) and its projection on the XY plane (right).

5.0.4 Fourth experiment

In this experiment we want to verify the wobbling when a propeller is detached from the hull. This is in an asymmetric situation which eventually can lead to less desired trajectories. Moreover, we can compare this setup with the one in which one propeller is switched off but not detached.
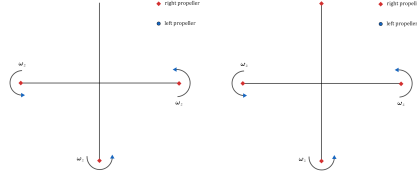

Figure 5.7: XY plane for the propulsive system

The first trajectory (in blue) clearly exhibits more wobbling than the second one, and at the same time it reaches greater distances, due to the lower resistance encountered during the motion ascribed to the lack of one propeller. The second configuration allows the robot to stay closer to the longitudinal axis but losing velocity. Due to the asymmetry of the problem, both trajectories are not parallel to the z-axis, as displayed in 5.8 left.

$$
\begin{bmatrix} v_x \\ v_y \\ v_z \\ \Omega_{hull,x} \\ \Omega_{hull,y} \\ \Omega_{hull,z} \end{bmatrix} = \begin{bmatrix} 6.8 \cdot 10^{-4} \\ -1 \cdot 10^{-3} \\ 3.1 \cdot 10^{-3} \\ 6.7 \cdot 10^{-4} \\ 1.2 \cdot 10^{-3} \\ 6.9 \cdot 10^{-3} \end{bmatrix}, \qquad \begin{bmatrix} v_x \\ v_y \\ v_z \\ \Omega_{hull,x} \\ \Omega_{hull,y} \\ \Omega_{hull,z} \end{bmatrix} = \begin{bmatrix} 5.6 \cdot 10^{-4} \\ -8.9 \cdot 10^{-4} \\ 2.6 \cdot 10^{-3} \\ 6.7 \cdot 10^{-4} \\ 9.9 \cdot 10^{-4} \\ 6.8 \cdot 10^{-3} \end{bmatrix} \tag{5.13}
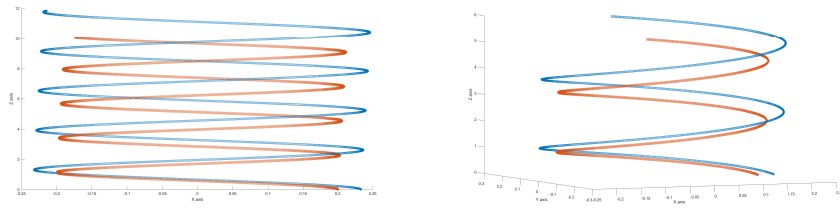$$

Figure 5.8: Experiment 4 - XZ section plane (left) and 3D trajectory (right)

5.0.5 Fifth experiment

Here, we want to compare the trajectories of the left configuration presented in experiment three with the micro-robot we were inspired by, that is the one presented by De Simone et al. [22] which is composed by one co-axial propeller only.
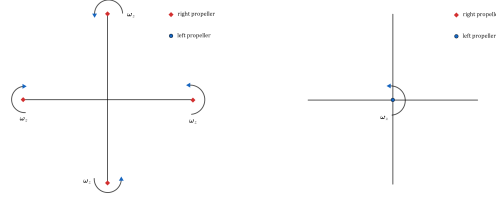

Figure 5.9: XY plane for the propulsive system

It is evident how the propellers arrangement in figure 5.9 (left) enables to reduce the wobbling with respect to the other case(red trajectory), therefore to achieve greater controllability.

$$
\begin{bmatrix} v_x \\ v_y \\ v_z \\ \Omega_{hull,x} \\ \Omega_{hull,y} \\ \Omega_{hull,z} \end{bmatrix} = \begin{bmatrix} 3.7 \cdot 10^{-4} \\ -6.6 \cdot 10^{-4} \\ 1.7 \cdot 10^{-3} \\ 4.5 \cdot 10^{-4} \\ 6.6 \cdot 10^{-4} \\ 4.5 \cdot 10^{-3} \end{bmatrix}, \quad \begin{bmatrix} v_x \\ v_y \\ v_z \\ \Omega_{hull,x} \\ \Omega_{hull,y} \\ \Omega_{hull,z} \end{bmatrix} = \begin{bmatrix} 2.9 \cdot 10^{-4} \\ -4.7 \cdot 10^{-4} \\ 1.6 \cdot 10^{-3} \\ 3 \cdot 10^{-4} \\ 5.2 \cdot 10^{-4} \\ 2.4 \cdot 10^{-3} \end{bmatrix} \tag{5.14}
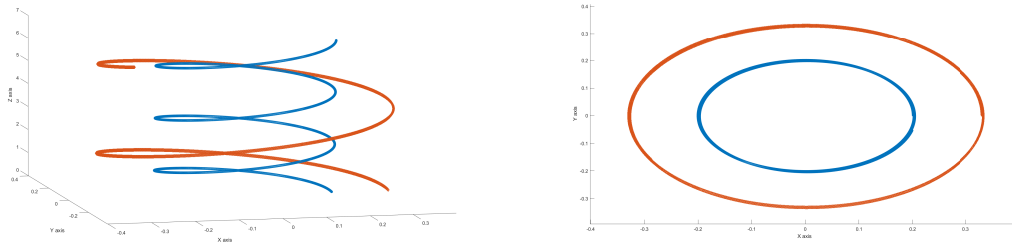$$

Figure 5.10: Experiment 6 - 3D trajectory & XY section plane

5.0.6 Sixth experiment

To further reduce wobbling by using the set up exploited in figure 5.9 left, one of the three anti-clockwise rotors can be switched off, as the configuration on the right side of figure 5.11 depicts

Figure 5.11: XY plane for the propulsive system

As reported in the velocity fields below, a reduction by almost half of the hull's rotational velocity is obtained. Also translational velocities are reduced.

$$
\begin{bmatrix} v_x \\ v_y \\ v_z \\ \Omega_{hull,x} \\ \Omega_{hull,y} \\ \Omega_{hull,z} \end{bmatrix} = \begin{bmatrix} 3.7 \cdot 10^{-4} \\ -6.6 \cdot 10^{-4} \\ 1.7 \cdot 10^{-3} \\ 4.5 \cdot 10^{-4} \\ 6.6 \cdot 10^{-4} \\ 4.5 \cdot 10^{-3} \end{bmatrix}, \quad \begin{bmatrix} v_x \\ v_y \\ v_z \\ \Omega_{hull,x} \\ \Omega_{hull,y} \\ \Omega_{hull,z} \end{bmatrix} = \begin{bmatrix} 1.8 \cdot 10^{-4} \\ -2.5 \cdot 10^{-4} \\ 8.8 \cdot 10^{-4} \\ 2.2 \cdot 10^{-4} \\ 3.2 \cdot 10^{-4} \\ 2.2 \cdot 10^{-3} \end{bmatrix} \tag{5.15}
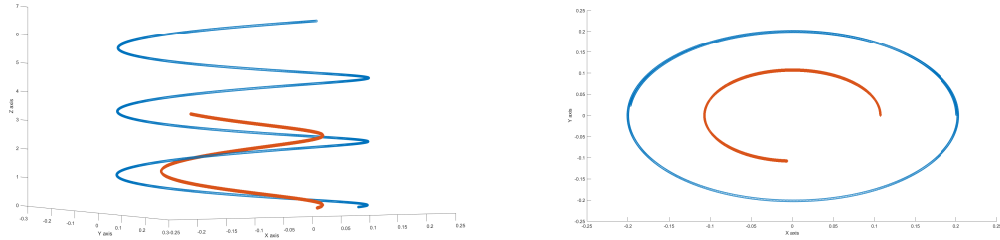$$

Figure 5.12: Experiment 7 - 3D trajectory(left) and its projection on the XY plane (right).

Figure 5.13 qualitatively describes, from the laboratory frame perspective, the behavior of the orthonormal triplet integral with the body during the translation of the micro-robot for a simulation time $t = 2500$. It is possible to note that the second configuration in figure 5.11 leads to a straighter trajectory(red), especially along the main translational axis.
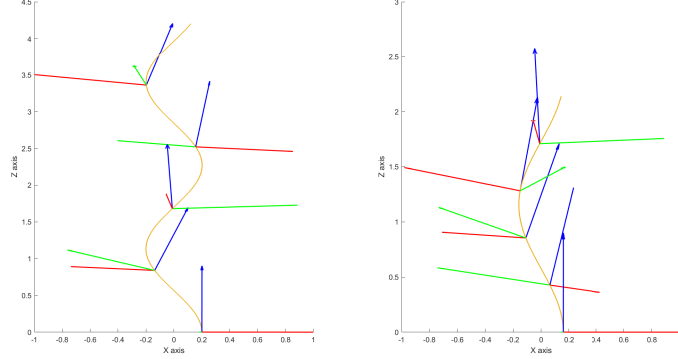
Figure 5.13: Orthonormal basis evolution along the section plane XZ

5.0.7 Seventh experiment

Finally, we want to compare our best configuration with the one proposed by De Simone et al in [22], showing the trajectories and the triplet, in order to understand which of the two configurations lead to less wobbling and less rotational velocity.
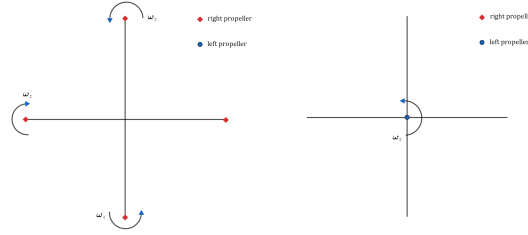

Figure 5.14: XY plane for the propulsive system

The configuration depicted in 5.14 (left) gives the blue trajectory while the other is showed in red. We can see how much the radius of curvature is reduced in figure 5.15 when adopting our micro-robot with respect to the one with only one co-axial helix. Furthermore, we also managed to reduce the magintude of the angular velocity, and this is highlighted in the numerical values of the last three components of the velocity vectors.

$$
\begin{bmatrix} v_x \\ v_y \\ v_z \\ \Omega_{hull,x} \\ \Omega_{hull,y} \\ \Omega_{hull,z} \end{bmatrix} = \begin{bmatrix} 1.8 \cdot 10^{-4} \\ -2.5 \cdot 10^{-4} \\ 8.8 \cdot 10^{-4} \\ 2.2 \cdot 10^{-4} \\ 3.2 \cdot 10^{-4} \\ 2.2 \cdot 10^{-3} \end{bmatrix}, \quad \begin{bmatrix} v_x \\ v_y \\ v_z \\ \Omega_{hull,x} \\ \Omega_{hull,y} \\ \Omega_{hull,z} \end{bmatrix} = \begin{bmatrix} 2.9 \cdot 10^{-4} \\ -4.7 \cdot 10^{-4} \\ 1.6 \cdot 10^{-3} \\ 3 \cdot 10^{-4} \\ 5.2 \cdot 10^{-4} \\ 2.4 \cdot 10^{-3} \end{bmatrix} \tag{5.16}
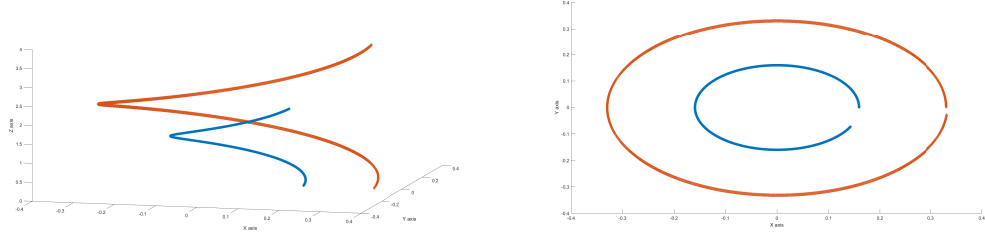$$

Figure 5.15: Experiment 7 - 3D trajectory(left) and its projection on the XY plane (right).

This last picture qualitatively shows the behaviour of the orthonormal triplet fixed on the body from the lab frame viewpoint during the translation of the micro-robot for a simulation time $t = 2000$. The triplets are only displayed for some time instants: $t_i = 1, 250, 500, 750, 1000, 1250, 1500$ and 1750.
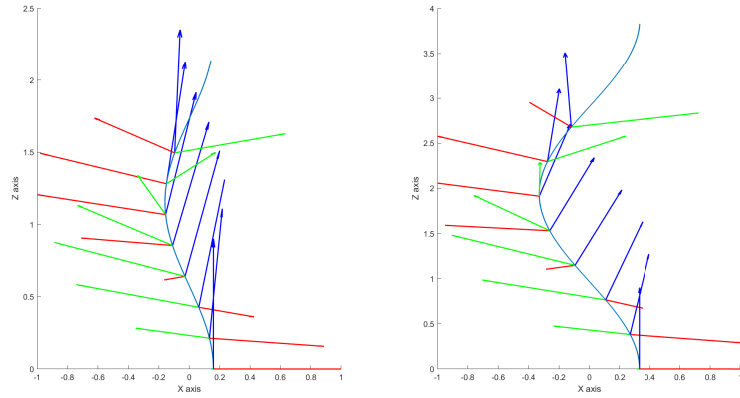

Figure 5.16: Orthonormal basis evolution along the section plane XZ

In conclusion, we deduced that the micro-robot with four propeller is more stable, i.e. has a minor radius of curvature, hence its trajectory is more in line with the z-axis and also its hull angular velocity is reduced. Given the symmetry of the problem we can avoid simulating the test cases which involves all the presented configurations with opposite direction of the angular velocity.

Chapter 6

Conclusions

In this thesis it was argued how the angular velocity and geometry of propellers can affect the motion of the micro-robot. It has been shown that certain configurations are more suitable than others to reduce wobbling with respect to the classical micro-robot presented in [22]. Furthermore it is made an overview of the other possible scenario to be encountered such as the loss of a propeller. A mathematical model of the hypothetical bio-inspired micro-robot was developed in order to understand the main aspects of kinematics and dynamics. The fluid dynamics around the geometry has been solved in Python with the open source computing platform FEniCSx. Two benchmark cases were used to validate this code: a sphere and an ellipsoid, whose coefficients can be calculated using analytical formulas. The results were encouraging, in fact a maximum error on certain resistance coefficients of 10% was obtained, although a coarse mesh was used, due to the limited computational resources. In addition, one more simulation was performed with a finer mesh, resulting in an error reduction of up to a maximum 2.5% on the same values. Once the code was validated, we obtained the coefficients of resistance for the propulsive system, composed of four propellers, and for the cargo, called hull. Thus, the matrices were assembled and their structure was similar as expected from the theory. The terms expected to be zero presented non zero values, still they were three orders of magnitude less than the other coefficients. This can also be attributed to the fact that the analytical values and the structures of the matrices are computed for the situation in which the flow is not confined, while we had to simulate on a computational domain, expressly chosen 80 times the maximum body size. Once the dynamics was solved we were able to obtain the translational and rotational velocities of the hull, therefore we can represent its trajectory for different input velocities and chirality of the propellers, finding the best configuration in order to reduce wobbling. This work has been done with the purpose of providing both theoretical and practical support through the model and simulations. The hope is being able to build such technologies in the near future, especially in biomedical contexts such as drug delivery or microsurgery. The field of research is very recent and the potentialities of improvement are many and touch various sectors, for example it would be interesting to equip the micro-robot with a camera able to do "image-detection" and an automatic control system capable to track a trajectory.

Bibliography

[1] Life at low Reynolds numbers. E.M Purcell. American Institute of Physics (1976)

[2] Swimming in circles: Motion of bacteria near solid boundaries. Eric Lauga, Willow R. DiLuzio, George M. Whitesides and Howard A. Stone. Biophysical Journal (2006).

[3] The efficiency of propulsion by a rotating flagellum. E.M Purcell. National Academy of Sciences (1997).

[4] Bioinspired reorientation strategies for application in micro/nanorobotic control. Ali Ghanbari. Journal of Micro-Bio Robotics (2006).

[5] Predicting and Optimizing Microswimmer Performance from the Hydrodynamics of Its Components: The Relevance of Interactions. Nicola Giuliani, Luca Heltai, and Antonio DeSimone. Soft Robotics (2018).

[6] Quadcopter Dynamics, Simulation, and Control Introduction Quadcopter Dynamics. Gibiansky A. (2012).

[7] Quadrotor control: modeling, nonlinear control design, and simulation. Francesco Sabatino. Master thesis at KTH electrical engineering, Stockholm (2015)

[8] Hydrodynamic interactions between rotating helices. MunJu Kim and Thomas R. Powers. Phys Rev E Stat Nonlin Soft Matter Phys. 2004

[9] An introduction to continuum mechanics. Morton E. Gurtin. Mathematics in science and engineering (1981).

[10] Meccanica razionale per l'ingegneria. V. Franceschini, C. Vernia. Pitagora Editrice Bologna (2011).

[11] Classical mechanics. Joel A. Shapiro. Rutgers, The State University of New Jersey .October 2010.

[12] Physical Fluid Dynamics. D. J. Tritton. Oxford Science Publications (1977).

[13] Modelling fluid structure interaction problems using boundary element method. Giuliani Nicola. Scuola Internazionale Superiore degli Studi Avanzati (2016).

[14] Stability and control of a quadrocopter despite the complete loss of one, two, or three propellers. Mark W. Mueller and Raffaello D'Andrea. IEEE International Conference on Robotics and Automation (2014).

[15] On the orientation of ellipsoidal particles in turbolent shear flow. Jurriaan J. J. Gillissen & B. J. Boersma. (2007)

[16] Effects of Hydrodynamic Interactions on the Near-Surface Diffusion of Spheroidal Molecules.Paweł Czajka, Jan M. Antosiewicz, and Maciej Długosz.ACS Omega 2019 4 (16), 17016-17030

[17] Hydrodynamic resistance of particles at small Reynolds numbers. Howard Brenner. Advances in chemical engineering (1966)

[18] Low Reynolds number hydrodynamics with special applications to particulate media. J.Happel, H.Brenner. ISBN: 978-90-247-2877-0. 1983

[19] Laminar flow and convective transport process: scaling principles and asymptotic analysis. L. Gary Leal. Butterworth-Heinemann. 1992

[20] Microhydrodynamics: principles and selected applications. S. Kim,S. J. Karrila. Butterworth-Heinemann. 1991

[21] Chemotaxis of bracken spermatozoids: Implications of electrochemical. Brokaw, C. J. J. exp. Biol. 35, 197-212. 1958b orientation.

[22] Planning a fantastic voyage: performance prediction and design of robotic micro-swimmers. G. Corsi. G. Noselli. A. DeSimone. SISSA, International School for Advanced Studies. 2021

[23] Mixed Finite Element Methods and Applications. Daniele Boffi, Franco Brezzi, Michel Fortin. Springer Series in Computational Mathematics, Vol. 44 (2013).

[24] C. Geuzaine and J.-F. Remacle. Gmsh: a three-dimensional finite element mesh generator with built-in pre- and post-processing facilities. International Journal for Numerical Methods in Engineering 79(11), pp. 1309-1331, 2009

[25] Ahrens, James, Geveci, Berk, Law, Charles, ParaView: An End-User Tool for Large Data Visualization, Visualization Handbook, Elsevier, 2005, ISBN-13: 978-0123875822

[26] Hassan Masoud, H. Stone .The reciprocal theorem in fluid dynamics and transport phenomena. Journal of Fluid Mechanics(2019).

[27] Rajesh Singh,1 Somdeb Ghose,1 and R. Adhikari1. Many-body microhydro-dynamics of colloidal particles with active boundary layers. The Institute of Mathematical Sciences, CIT Campus, Chennai 600113, India.

[28] Howard Brenner. The slow motion of a sphere through a viscous fluid towards a plane surface. Chemical Engineering Science. Volume 16, Issues 3–4. 1961.

[29] Philip C Nelson. Biological Physics: Energy, Information, Life. W. H. Freeman and Co.

[30] Zhong, Shan and Moored, Keith and Pinedo, Victor and Garcia-Gonzalez, Jesus and Smits, Alexander. The flow field and axial thrust generated by a rotating rigid helix at low Reynolds numbers. Experimental Thermal and Fluid Science. 2013

[31] Manickam Siva Kumar, Pichai Philominatha. Computational Fluid Dynamics Modeling Studies on Bacterial Flagellar Motion. International Journal of Fluid Machinery and Systems. Vol. 4, No. 3, July-September 2011

[32] Shan Zhong, Keith W. Moored, Victor Pinedo, Jesus Garcia-Gonzalez, Alexander J. Smits. The flow field and axial thrust generated by a rotating rigid helix at low Reynolds numbers. Experimental Thermal and Fluid Science. Volume 46, 2013.

[33] Hugh C. Crenshaw, Leah Edelstein-Keshet. Orientation by helical motion—II. Changing the direction of the axis of motion. Bulletin of Mathematical Biology. Volume 55, Issue 1. 1993

[34] M. W. Scroggs, J. S. Dokken, C. N. Richardson, and G. N. Wells. Construction of arbitrary order finite element degree-of-freedom maps on polygonal and polyhedral cell meshes, to appear in ACM Transactions on Mathematical Software (2022).

[35] M. W. Scroggs, I. A. Baratta, C. N. Richardson, and G. N. Wells. Basix: a runtime finite element basis evaluation library, submitted to Journal of Open Source Software (2022).

[36] A. Logg, K.-A. Mardal, G. N. Wells et al. Automated Solution of Differential Equations by the Finite Element Method, , Springer(2012).

[37] A. Logg, G. N. Wells and J. Hake. DOLFIN: a C++/Python Finite Element Library, in: A. Logg, K.-A. Mardal and G. N. Wells (eds) Automated Solution of Differential Equations by the Finite Element Method (chapter 10), volume 84 of Lecture Notes in Computational Science and Engineering, Springer (2012).

[38] Andersson, Helge and Jiang, Fengjian. Forces and torques on a prolate spheroid: low-Reynolds-number and attack angle effects. Acta Mechanica. 2019

[39] Hameed, Muna and Jassim, Lina and Alguboori, Atheer and Habeeb, Laith and Kareem, Humam. Porosity Influence on Natural Convection Heat Transfer from a Heated Cylinder in a Square Porous Enclosure. Journal of Mechanical Engineering Research and Developments. 2020

[40] Maciej Lisicki and Shang Yik Reigh and Eric Lauga. Autophoretic motion in three dimensions. Soft matter (2018).